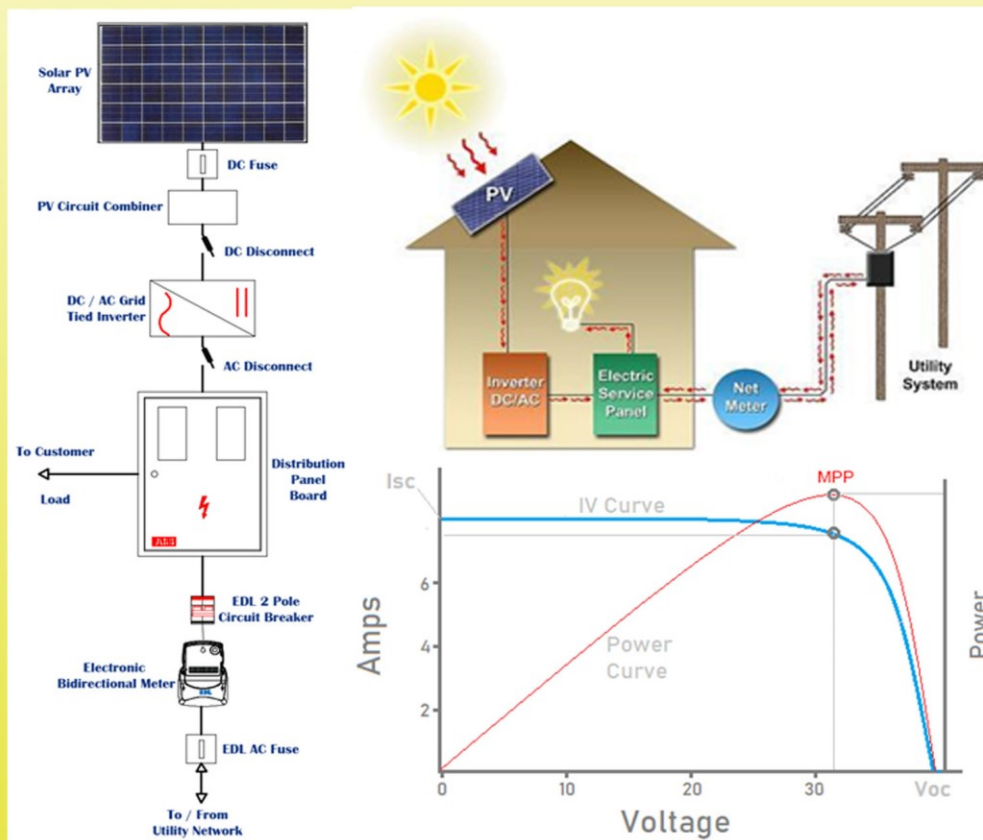


Trends in Renewable Energy

Volume 6, Issue 3, December 2020



Cover image: Net Metering in Lebanon, see article by Shabani and Chaaban in this issue.



Trends in Renewable Energy

ISSN: 2376-2136 (Print) ISSN: 2376-2144 (Online)

<http://futureenergysp.com/>

Trends in Renewable Energy is an open accessed, peer-reviewed semi-annual journal publishing reviews and research papers in the field of renewable energy technology and science.

The aim of this journal is to provide a communication platform that is run exclusively by scientists working in the renewable energy field. Scope of the journal covers: Bioenergy, Biofuel, Biomass, Bioprocessing, Biorefinery, Biological waste treatment, Catalysis for energy generation, Energy conservation, Energy delivery, Energy resources, Energy storage, Energy transformation, Environmental impact, Feedstock utilization, Future energy development, Green chemistry, Green energy, Microbial products, Physico-chemical process for Biomass, Policy, Pollution, Renewable energy, Smart grid, Thermo-chemical processes for biomass, etc.

The Trends in Renewable Energy publishes the following article types: peer-reviewed reviews, mini-reviews, technical notes, short-form research papers, and original research papers.

The article processing charge (APC), also known as a publication fee, is fully waived for the Trends in Renewable Energy.

Editorial Team of Trends in Renewable Energy

EDITOR-IN-CHIEF

Dr. Bo Zhang

Prof., School of Chemical Engineering & Pharmacy, Wuhan Institute of Technology, China

Dr. Changyan Yang

Prof., School of Chemical Engineering & Pharmacy, Wuhan Institute of Technology, China

HONORARY CHAIRMEN

Dr. Yong Wang

Voiland Distinguished Professor, The Gene and Linda Voiland School of Chemical Engineering and Bioengineering, Washington State University, United States

Dr. Mahendra Singh Sodha

Professor, Lucknow University; Former Vice Chancellor of Devi Ahilya University, Lucknow University, and Barkatulla University; Professor/Dean/HOD/Deputy Director at IIT Delhi; Padma Shri Award; India Professor of Industrial Chemistry, CEO of Eurochem Engineering srl, Italy

Dr. Elio Santacesaria

VICE CHAIRMEN

Dr. Mo Xian

Prof., Assistant Director, Qingdao Institute of BioEnergy and Bioprocess Technology, Chinese Academy of Sciences, China

EDITORS

Dr. Yiu Fai Tsang,

Associate Prof., Department of Science and Environmental Studies, The Education University of Hong Kong

Dr. Melanie Sattler

Dr. Syed Qasim Endowed Professor, Dept. of Civil Engineering, University of Texas at Arlington, United States

Dr. Attila Bai

Associate Prof., University of Debrecen, Hungary

Prof. Christophe Pierre Ménézo

University of Savoy Mont-Blanc, France

Dr. Moinuddin Sarker

MCIC, FICER, MInstP, MRSC, FARSS., VP of R & D, Head of Science/Technology Team, Natural State Research, Inc., United States Associate Prof., Biomass Processing Laboratory, Centre for Biofuel and Biochemical Research, Green Technology Mission Oriented Research, Universiti Teknologi PETRONAS, Malaysia

Dr. Suzana Yusup

Global Technology Development, Monsanto Company, United States

Dr. Zewei Miao

Pfizer Inc., United States

Dr. Hui Wang

North Carolina Agricultural and Technical State University, United States

Dr. Shuangning Xiu

Associate Prof., Institute of Chemical Industry of Forest Products, China

Dr. Junming XU

Academy of Forest, China

Dr. Hui Yang

Prof., College of Materials Science and Engineering, Nanjing Tech University, China

Dr. Ying Zhang

Associate Prof., School of Chemistry and Materials Science, University of Science and Technology of China, China

Dr. Ming-Jun Zhu

Prof., Assistant Dean, School of Bioscience & Bioengineering, South China University of Technology, China

EDITORIAL BOARD

Dr. Risabh Dev Shukla

Dean and Associate Prof., Department of Electrical Engineering, Budge Budge Institute of Technology Kolkata, India

Dr. Neeraj Gupta

Indian Institute of Technology Roorkee, India

Dr. Elena Lucchi	Politecnico di Milano, Italy
Dr. Muhammad Mujtaba Asad	Faculty of Technical and Vocational Education, Universiti Tun Hussein Onn Malaysia, Malaysia
Dr. Afzal Sikander	Department of Instrumentation and Control Engineering, Dr. B. R. Ambedkar National Institute of Technology, India
Dr. Padmanabh Thakur	Professor and Head, Department of Electrical Engineering, Graphic Era University, India
Dr. K. DHAYALINI	Professor, Department of Electrical and Electronics Engineering, K. Ramakrishnan College of Engineering, Tamilnadu, India
Shangxian Xie	Texas A&M University, United States
Dr. Tanmoy Dutta	Sandia National Laboratories, United States
Dr. Efsthios Stefanos	Pontifical Catholic University of Ecuador, Faculty of Exact and Natural Sciences, School of Physical Sciences and Mathematics, Ecuador
Dr. Xin Wang	Miami University, United States
Dr. Rami El-Emam	Assist. Prof., Faculty of Engineering, Mansoura University, Egypt
Dr. Rameshprabu Ramaraj	School of Renewable Energy, Maejo University, Thailand
Dr. ZAFER ÖMER ÖZDEMİR	Kirklareli University, Technology Faculty, Turkey
Dr. Vijay Yeul	Chandrapur Super Thermal Power Station, India
Dr. Mohanakrishna Gunda	VITO - Flemish Institute for Technological Research, Belgium
Dr. Shuai Tan	Georgia Institute of Technology, United States
Shahabaldin Rezanian	Universiti Teknologi Malaysia (UTM), Malaysia
Dr. Madhu Sabnis	Contek Solutions LLC, Texas, United States
Dr. Qiang Yan	Mississippi State University, United States
Dr. Mustafa Tolga BALTA	Associate Prof., Department of Mechanical Engineering, Faculty of Engineering, Aksaray University, Turkey
Dr. María González Alriols	Associate Prof., Chemical and Environmental Engineering Department, University of the Basque Country, Spain
Dr. Nattaporn Chaiyat	Assist. Prof., School of Renewable Energy, Maejo University, Thailand
Dr. Nguyen Duc Luong	Institute of Environmental Science and Engineering, National University of Civil Engineering, Vietnam
Mohd Lias Bin Kamal	Faculty of Applied Science, Universiti Teknologi MARA, Malaysia
Dr. N.L. Panwar	Assistant Prof., Department of Renewable Energy Engineering, College of Technology and Engineering, Maharana Pratap University of Agriculture and Technology, India
Dr. Caio Fortes	BASF, Brazil
Dr. Flavio Praticco	Department of Methods and Models for Economics, Territory and Finance, Sapienza University of Rome, Italy
Dr. Wennan ZHANG	Docent (Associate Prof.) and Senior Lecturer in Energy Engineering, Mid Sweden University, Sweden
Dr. Ing. Stamatis S. Kalligeros	Associate Prof., Hellenic Naval Academy, Greece
Carlos Rolz	Director of the Biochemical Engineering Center, Research Institute at Universidad del Valle, Guatemala
Ms. Liliash Makashini	Copperbelt University, Zambia
Dr. Ali Mostafaeipour	Assistant Prof., Industrial Engineering Department, Yazd University, Iran
Dr. Camila da Silva	Prof., Maringá State University, Brazil
Dr. Anna Skorek-Osikowska	Silesian University of Technology, Poland
Dr. Shek Atiqure Rahman	Sustainable and Renewable Energy Engineering, College of Engineering, University of Sharjah, Bangladesh
Dr. Emad J Elnajjar	Associate Prof., Department of Mechanical Engineering, United Arab Emirates University, United Arab Emirates
Dr. Seyed Soheil Mousavi Ajarostaghi	Babol Noshirvani University of Technology, Babol, Iran
Dr. Dinesh K. Sharma	National Ecology and Environment Foundation, India
Dr. Lakshmana Kumar Ramasamy	Department of Corporate relations, Hindusthan College of Engineering and Technology, India
Dr. S. Venkata Ramana	SUSU/National Research University, Russian Federation
Dr. Priyanka Marathey	Department of Solar Energy, Pandit Deendayal Petroleum University, India
Osamah Siddiqui	University of Ontario Institute of Technology, Canada

Dr. Rupendra Kumar Pachauri	Assistant Prof., Electrical and Electronics Engineering Department, University of Petroleum and Energy Studies, India
Dr. Jun Mei	School of Chemistry and Physics, Science and Engineering Faculty, Queensland University of Technology, Australia
Dr. Valeria Di Sarli	Institute for Research on Combustion, National Research Council of Italy, Italy
Dr. Utkucan Şahin	Assistant Prof., Department of Energy Systems Engineering, Faculty of Technology, Muğla Sıtkı Koçman University, Turkey
Dr. ALIASHIM ALBANI	School of Ocean Engineering, Universiti Malaysia Terengganu, Malaysia
Dr. Ashwini Kumar	Assistant Prof., College of Engineering, HSBPVT's Parikrama Group of Institutions, India
Dr. Hasan AYDOGAN	Associate Prof., Mechanical Engineering Department, Selcuk University, Turkey
Dr. Jiekang Wu	Professor, School of Automation, Guangdong University of Technology, China
Dr. Ong Huei Ruey	DRB-HICOM University of Automotive, Malaysia
Dr. Miguel Ángel Reyes Belmonte	IMDEA Energy Institute, Spain
Dr. Chitra Venugopal	Associate Professor in Electrical Engineering, University of Trinidad and Tobago, Trinidad
Dr. Amit Kumar Singh	Assistant Prof., Instrumentation & Control Engineering Department, Dr. B.R.A. National Institute of Technology, India
Dr. Suvanjan Bhattacharyya	University of Pretoria, South Africa
Dr. Karunesh Tiwari	Babu Banarasi Das University, India
Dr. Sharadrao A. Vhanalkar	Karmaveer Hire Arts, Science, Commerce and Education College, India
Dr. Prasenjit Chatterjee	Assistant Prof. and Head, MCKV Institute of Engineering, India
Dr. S. Balamurugan	Mindnotix Technologies, India
Dr. Mohammad Nurunnabi	University of Oxford, United Kingdom
Dr. Kenneth Okedu	Caledonian College of Engineering, Oman
Dr. Cheng Zhang	Sr. Materials Engineer, Medtronic, Inc., United States
Dr. Chandani Sharma	Assistant Prof., Department of Electrical Engineering, Graphic Era University, India
Dr. Kashif Irshad	Assistant Prof., Mechanical Engineering Department, King Khalid University, Saudi Arabia
Dr. Abhijit Bhagavatula	Principal Lead Engineer, Southern Company Services, United States
Dr. S. Sathish	Associate Prof., Department of Mechanical Engineering, Hindustan University, India
Mr. A. Avinash	Assistant Prof., KPR Institute of Engineering & Technology, India
Dr. Bindeshwar Singh	Assistant Prof., Kamla Nehru Institute of Technology, India
Dr. Yashar Hashemi	Tehran Regional Electric Company, Iran
Dr. Navanietha Krishnaraj R	South Dakota School of Mines and Technology, United States
Dr. SANDEEP GUPTA	JECRC University, India
Dr. Shwetank Avikal	Graphic Era Hill University, India
Dr. Xianglin Zhai	Poochon Scientific LLC, United States
Dr. Rui Li	Associate Prof., College of Engineering, China Agricultural University, China
Dr. Adam Elhag Ahmed	National Nutrition Policy Chair, Department of Community Services, College of Applied Medical Sciences, King Saud University, Saudi Arabia
Dr. Jingbo Li	Massachusetts Institute of Technology, United States
Dr. Srikanth Mutnuri	Associate Prof., Department of Biological Sciences, Associate Dean for International Programmes and Collaboration, Birla Institute of Technology & Science, India
Dr. Bashar Malkawi	Global Professor of Practice in Law, James E. Rogers College of Law, University of Arizona, United States
Dr. Simona Silvia Merola	Istituto Motori - National Research Council of Naples, Italy
Dr. Hakan Caliskan	Faculty of Engineering, Department of Mechanical Engineering, Usak University, Turkey
Dr. Umashankar Subramaniam	Associate Prof., College of Engineering, Prince Sultan University, Saudi Arabia
Dr. Tayfun GÜNDOĞDU	Faculty of Electrical and Electronic Engineering, Department of Electrical Engineering, Istanbul Technical University, Turkey
Dr. Yukesh Kannah R	Department of Civil Engineering, Anna University Regional Campus, India

Table of Contents

Volume 6, Issue No. 3, December 2020

Articles

Process Design of Microalgae Slurry Pump

Jiayi Li, Yinhang Qu, Yu Gong, Changyan Yang, Bohan Yang, Peng Liu, Bo Zhang, Yigang Ding234-244

Management Information Systems and Data Science in the Smart Grid – Inner Class Area Capacity

Distribution of the iSHM Class Maps of Overhead Low-Voltage Broadband over Power Lines

Topologies

Athanasios G. Lazaropoulos245-265

Technical Overview of the Net Metering in Lebanon

Issam Shabani, Mohammad Chaaban.....266-284

Process Design of Microalgae Slurry Pump

Jiayi Li^{1,a}, Yinhang Qu^{1,a}, Yu Gong^{1,a}, Changyan Yang^{1,2*}, Bohan Yang¹, Peng Liu¹, Bo Zhang^{1*}, Yigang Ding¹

1: Key Laboratory for Green Chemical Process of Ministry of Education, Hubei Key Laboratory of Novel Chemical Reactor and Green Chemical Technology, School of Chemical Engineering and Pharmacy, Wuhan Institute of Technology, Hubei, China

2: Hubei Key Laboratory for Processing and Application of Catalytic Materials, Huanggang Normal University, Hubei, China

a: These three authors contribute to this work equally.

Received June 21, 2020; Accepted July 21 2020; Published July 25, 2020

Microalgae are a renewable source of dietary supplements, bioactive compounds, and potential energy. Once harvested, the microalgal medium is dewatered to form a slurry for downstream processing. This article outlines a process design for pumping the microalgae slurry. The pump requirements for delivering the *Chlorella* slurry with 5, 10 or 20 wt% solids at one tonne per hour (1,000 kg/h) and 10 bar were calculated. The 5 wt% microalgae slurry is a Newtonian fluid with a viscosity of 1.95 mPa·s. The 10 wt% and 20 wt% microalgae slurries are non-Newtonian fluids, whose viscosity depends on the shear rate (γ). The viscosity of 10 wt% and 20 wt% microalgae slurries is $1.504 (\gamma = 50 \text{ s}^{-1})/1.155 (\gamma = 100 \text{ s}^{-1})$ and $1.844 (\gamma = 50 \text{ s}^{-1})/1.219 (\gamma = 100 \text{ s}^{-1})$ mPa·s, respectively. The pump power requirements are mainly governed by the delivery pressure. The effect of the pipe length and the number of elbows is negligible. The effective power of the pump is calculated as 0.267-0.275 kW. To fulfill this duty, a ZGB type single-stage single-suction centrifugal slurry pump can be selected, which would provide enough shear rate to reduce the viscosity of the microalgae slurry and give required shaft power.

Keywords: Microalgae Slurry; Slurry Pump; Process Design; Viscosity; Pump Power

Introduction

Microalgae are a source of dietary supplements, bioactive compounds, and potential energy, which have been invested extensively [1, 2]. Generally, the microalgal culture has a very dilute concentration of 0.1-0.5 wt% dry solids [3]. Currently, the proposed harvesting process is using a series of mechanical unit operations to dewater the microalgae medium to a level of ~20 wt% dry solids [4], which is considered as a less energy intensive processing option than completely drying microalgae [5]. The slurry after dewatering is considerably more viscous, but it is still a flowable slurry. Thus, it only needs to be transported to downstream processing facility using a slurry pump. Downstream

*Corresponding author: ychy1969@163.com, bzhang_wh@foxmail.com

processing of microalgae may include drying [6], extraction to yield biochemicals [7], and hydrothermal liquefaction [8] or pyrolysis to produce bio-fuels [9, 10]. The slurry pump is the key equipment for transporting the feedstock.

This paper provides a simple process design for pumping microalgae slurry. The purpose is to provide a tutorial for calculating the power requirement for pumping of various microalgae slurries, and provide data support when selecting pumps. The effect of the pipe length and the number of elbows was also discussed.

Methodology

Process Description

A microalgae flow is pumped by a slurry pump from a storage tank to the downstream processing facility. The process is illustrated in Figure 1, in which the processing facility is assumed to be a drying unit. The calculation of the drying process is not within the scope of this article.

The flow rate of the microalgal slurry is 1,000 kg/h, and the solid content is 5 wt%, 10 wt% or 20 wt%. The temperature of the slurry is 25°C and the pressure is 1 bar. The duty of the slurry pump is to pressurize the flow to 10 bar, and the efficiency of the pump is 70%. The slurry is delivered through 100 meters of PVC pipe (diameter 0.1 m) and three 90° elbows to the top of the dryer.

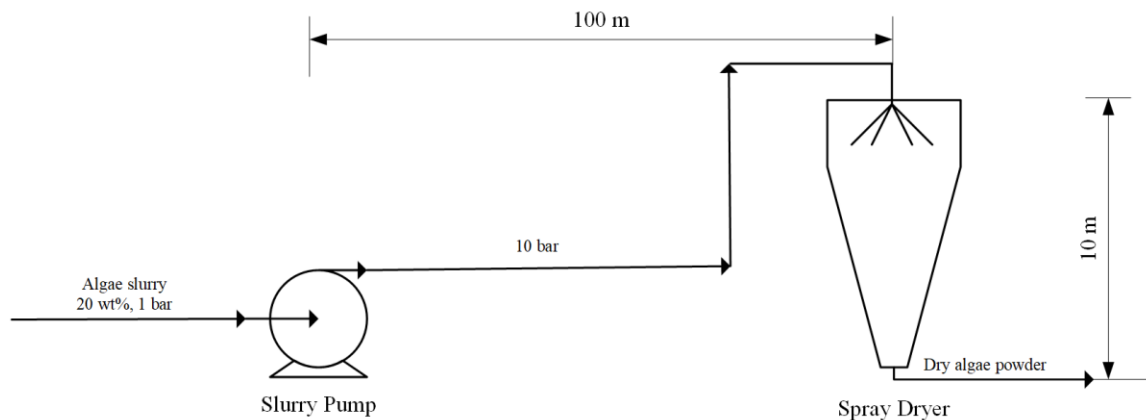


Figure 1. Process for microalgae pumping and drying

Microalgae

Green microalga *Chlorella sp.* is assumed to be grown autotrophically, harvested, and concentrated to a solid content of up to 20 wt% via a series of dewatering processes. The detailed design of the dewatering process can be found in the literature [3]. The elemental composition and biochemical components of *Chlorella sp.* have been summarized in our previous study [11].

Results and Discussion

Viscosity of 5, 10, and 20 wt% Microalgal Slurry

The *Chlorella* slurry with a solid content of 5 wt% is a Newtonian fluid. The viscosity can be calculated by the following formula [12]:

$$\mu_{eff} = 1.9 \times 10^{-5} \times C + 1.0 \times 10^{-3} \quad (1)$$

where μ_{eff} (Pa·s) is the effective viscosity, and C is the microalgae concentration and its unit is (kg/m³). Assuming the 5 wt% concentration is the percent weight/volume (% w/v), Equation 1 becomes:

$$\mu_{eff} = 1.9 \times 10^{-5} \times 50 + 1.0 \times 10^{-3} = 1.95 \text{ mPa} \cdot \text{s} \quad (2)$$

The *Chlorella* slurry with a solid content higher than 6 wt% is considered as non-Newtonian fluid. Its viscosity depends on the shear rate and follows the Herschel-Bulkley model:

$$\eta = K|\dot{\gamma}|^{n-1} + \tau_y|\dot{\gamma}|^{-1} \quad (3)$$

where η is the viscosity, τ_y is the yield stress, K is the consistency, n is the flow index, and $\dot{\gamma}$ is the shear rate [s⁻¹]. The Herschel-Bulkley parameters for the *Chlorella* slurry can be found in the literature as follows [13]:

Table 1. Herschel-Bulkley parameters for the *Chlorella* slurry

Solid content	10%	20%
τ_y (mPa)	50.56	80.1
K (MPa·S ⁿ)	0.103	0.011
n	1.4	1.79

For the 10 wt% microalgal slurry, when $\dot{\gamma}$ is 50 s⁻¹,

$$\eta = 0.103 \times 50^{1.4-1} + 50.56 \times 50^{-1} = 1.504 \text{ mPa} \cdot \text{s} \quad (4)$$

When $\dot{\gamma}$ is 100 s⁻¹,

$$\eta = 0.103 \times 100^{1.4-1} + 50.56 \times 100^{-1} = 1.155 \text{ mPa} \cdot \text{s} \quad (5)$$

For the 20 wt% microalgal slurry, when $\dot{\gamma}$ is 50 s⁻¹,

$$\eta = 0.011 \times 50^{1.79-1} + 80.1 \times 50^{-1} = 1.844 \text{ mPa} \cdot \text{s} \quad (6)$$

When $\dot{\gamma}$ is 100 s⁻¹,

$$\eta = 0.011 \times 100^{1.79-1} + 80.1 \times 100^{-1} = 1.219 \text{ mPa} \cdot \text{s} \quad (7)$$

Therefore, the viscosity of 5, 10, and 20 wt% *Chlorella* slurries was 1.95 mPa·s, 1.155 mPa·s (at $\dot{\gamma}=100$ s⁻¹), and 1.219 mPa·s (at $\dot{\gamma}=100$ s⁻¹), respectively. The viscosity of the microalgae slurry mainly depends on the fluid type.

Slurry Pump Design

This section calculates the power and equipment selection of the slurry pump. The calculation considers three kinds of algal slurry concentration, 100 meters of pipeline length, 10 meters of tower height, and three 90° right angle elbows. The density of *Chlorella* slurry is not available in the literature. Therefore, it is assumed that the density

of *Chlorella* slurry is similar to that of *Nannochloropsis salina* [14]. Therefore, the density of 5, 10, and 20 wt% microalgae slurries are 1,009, 1,020, and 1,042 kg/m³, respectively.

5 wt% Microalgae Slurry

The volumetric flow rate is calculated as:

$$q_v = \frac{q_m}{\rho} = \frac{1000}{1009} = 0.99 \text{ m}^3 / \text{h} \quad (8)$$

Flow velocity in the pipe is:

$$u = \frac{q_v}{\frac{\pi d^2}{4}} = \frac{0.991}{\frac{\pi}{4} \times 0.1^2} = 126.188 \text{ m/h} = 0.035 \text{ m/s} \quad (9)$$

Because the 5 wt% microalgal slurry belongs to Newtonian fluid, the viscosity is constant. So, Reynolds number (Re) is calculated as

$$\text{Re} = \frac{du\rho}{\mu} = \frac{0.1 \times 0.0351 \times 1009}{0.00195} = 1813.728 < 2000 \quad (10)$$

Reynolds number is less than 2000, so the fluid is a laminar flow. Friction coefficient is

$$\lambda = \frac{64}{\text{Re}} = \frac{64}{1813.728} = 0.0353 \quad (11)$$

According to the Chemical Engineering handbook [15], for the 90° elbow, the coefficient of local resistance and the equivalent length ratio are:

$$\zeta = 0.75 \quad (12)$$

$$\frac{l_e}{d} = 35 \quad (13)$$

The total resistance of the pipeline is:

$$\sum h_f = \left(\lambda \frac{\sum l_i}{d} + \sum \zeta_i \right) \frac{u^2}{2} = \left[0.0353 \times \left(\frac{100}{0.1} \right) + 3 \times 0.75 \right] \times \frac{0.0351^2}{2} = 0.0231 \text{ J/kg} \quad (14)$$

$$\sum H_f = \frac{\sum h_f}{g} = \frac{0.0231}{9.81} = 0.00236 \text{ m} \quad (15)$$

Assuming the horizontal pipe is the datum, Bernoulli equation is listed as:

$$z_1 + \frac{u_1^2}{2g} + \frac{p_1}{\rho g} + H_e = z_2 + \frac{u_2^2}{2g} + \frac{p_2}{\rho g} + \sum H_f \quad (16)$$

where, $z_2 - z_1 = 10 \text{ m}$, $u_1 = 0$, $u_2 = 0.0351 \text{ m/s}$, $P_1 = 1 \text{ bar}$, $P_2 = 10 \text{ bar}$

Pump head is calculated as

$$H_e = 10 + \frac{0.0351^2}{2 \times 9.81} + \frac{9 \times 10^5}{1009 \times 9.81} + 0.00236 = 100.927 \text{ m} \quad (17)$$

The effective power of the pump is

$$P_e = q_v \rho g H_e = \frac{0.991}{3600} \times 1009 \times 9.81 \times 100.927 = 0.275 \text{ kW} \quad (18)$$

The pump shaft power is

$$P = \frac{P_e}{\eta} = \frac{0.275}{0.7} = 0.393kW \quad (19)$$

10 wt% Microalgae Slurry

The volumetric flow rate is

$$q_v = \frac{q_m}{\rho} = \frac{1000}{1020} = 0.98m^3 / h \quad (20)$$

Flow velocity in the pipe:

$$u = \frac{q_v}{\frac{\pi}{4}d^2} = \frac{0.98}{\frac{\pi}{4} \times 0.1^2} = 124.891m / h = 0.0347m / s \quad (21)$$

Because the 10 wt% microalgal slurry is non-Newtonian fluid, when $\gamma = 50 \text{ s}^{-1}$, the viscosity η is 1.504 mPa·s. Reynolds number is

$$Re_t = \frac{du\rho}{\eta} = \frac{0.1 \times 0.0347 \times 1020}{1.504 \times 10^{-3}} = 2353.32 > 2000, \quad (22)$$

Reynolds number is higher than 2000, so the fluid is a turbulent flow. Then, the modified Blasius equation can be applied:

$$\lambda = \frac{a}{Re_t^b} \quad (23)$$

where turbulent constants a and b are the function of the flow behavior index (n) with $a = 0.3104n^{0.105}$, $b = 0.2495n^{-0.217}$, and $n=1.4$. Substitute these values into the equation to obtain $a=0.3216$, $b=0.232$, and $\lambda=0.0531$.

The total resistance of the pipeline is:

$$\sum H_f = \left(\lambda \sum \frac{l_i}{d} + \sum \zeta_i \right) \frac{u^2}{2g} = \left[0.0531 \times \left(\frac{100}{0.1} \right) + 3 \times 0.75 \right] \times \frac{0.0347^2}{2 \times 9.81} = 0.00339m \quad (24)$$

Bernoulli equation gives the pump head as:

$$H_e = 10 + \frac{0.0347^2}{2 \times 9.81} + \frac{9 \times 10^5}{1020 \times 9.81} + 0.00339 = 99.948m \quad (25)$$

The effective power of the pump is

$$P_e = q_v \rho g H_e = \frac{0.98}{3600} \times 1020 \times 9.81 \times 99.948 = 0.272kW \quad (26)$$

The pump shaft power is

$$P = \frac{P_e}{\eta} = \frac{0.272}{0.7} = 0.389kW \quad (27)$$

When $\gamma = 100 \text{ s}^{-1}$, the viscosity η is 1.155 mPa·s. Reynolds number is

$$Re_t = \frac{du\rho}{\eta} = \frac{0.1 \times 0.0347 \times 1020}{1.155 \times 10^{-3}} = 3064.42 > 2000 \quad (28)$$

The fluid is a turbulent flow. The modified Blasius equation gives

$\lambda = \frac{a}{\text{Re}_f^b}$, $a = 0.3104n^{0.105}$, $b = 0.2495n^{-0.217}$, $n=1.4$. Substitute these values into

the equation to obtain:

$$a=0.3216, b=0.232, \lambda=0.0499 \quad (29)$$

The total resistance of the pipeline is:

$$\sum H_f = \left(\lambda \frac{\sum l_i}{d} + \sum \zeta_i \right) \frac{u^2}{2g} = \left[0.0499 \times \left(\frac{100}{0.1} \right) + 3 \times 0.75 \right] \times \frac{0.0347^2}{2 \times 9.81} = 0.00321m \quad (30)$$

Bernoulli equation gives:

$$H_e = 10 + \frac{0.0347^2}{2 \times 9.81} + \frac{9 \times 10^5}{1020 \times 9.81} + 0.00321 = 99.948m \quad (31)$$

The effective power of the pump is

$$P_e = q_v \rho g H_e = \frac{0.98}{3600} \times 1020 \times 9.81 \times 99.948 = 0.272kW \quad (32)$$

The pump shaft power is

$$P = \frac{P_e}{\eta} = \frac{0.272}{0.7} = 0.389kW \quad (33)$$

20 wt% Microalgae Slurry

The volumetric flow rate is

$$q_v = \frac{q_m}{\rho} = \frac{1000}{1042} = 0.96m^3/h \quad (34)$$

Flow velocity in the pipe is

$$u = \frac{q_v}{\frac{\pi d^2}{4}} = \frac{0.96}{\frac{\pi}{4} \times 0.1^2} = 122.254m/h = 0.034m/s \quad (35)$$

Because the 20 wt% microalgal slurry is non-Newtonian fluid, when $\gamma = 50 \text{ s}^{-1}$, the viscosity η is 1.844 mPa·s. Reynolds number is

$$\text{Re}_f = \frac{du\rho}{\eta} = \frac{0.1 \times 0.034 \times 1042}{1.844 \times 10^{-3}} = 1921.25 < 2000 \quad (36)$$

Reynolds number is less than 2000, so the fluid is a laminar flow. Friction coefficient is

$$\lambda = \frac{64}{\text{Re}} = \frac{64}{1921.25} = 0.0333 \quad (37)$$

The total resistance of the pipeline is:

$$\sum H_f = \left(\lambda \frac{\sum l_i}{d} + \sum \zeta_i \right) \frac{u^2}{2g} = \left[0.0333 \times \left(\frac{100}{0.1} \right) + 3 \times 0.75 \right] \times \frac{0.034^2}{2 \times 9.81} = 0.00209m \quad (38)$$

According to the Bernoulli equation, the pump head is

$$H_e = 10 + \frac{0.034^2}{2 \times 9.81} + \frac{9 \times 10^5}{1042 \times 9.81} + 0.00209 = 98.048m \quad (39)$$

The effective power of the pump is

$$P_e = q_v \rho g H_e = \frac{0.96}{3600} \times 1042 \times 9.81 \times 98.048 = 0.267kW \quad (40)$$

The pump shaft power is

$$P = \frac{P_e}{\eta} = \frac{0.267}{0.7} = 0.382kW \quad (41)$$

When $\gamma = 100 \text{ s}^{-1}$, the viscosity η is 1.219 mPa·s. Reynolds number is

$$Re_l = \frac{du\rho}{\eta} = \frac{0.1 \times 0.034 \times 1042}{1.219 \times 10^{-3}} = 2906.32 > 2000 \quad (42)$$

Then, the modified Blasius equation is applied:

$$\lambda = \frac{a}{Re_l^b}, \quad a = 0.3104n^{0.105}, \quad b = 0.2495n^{-0.217}, \quad n = 1.79. \text{ Substitute these values into}$$

the equation to obtain $a=0.33$, $b=0.22$, and $\lambda=0.0571$.

The total resistance of the pipeline is

$$\sum H_f = \left(\lambda \frac{\sum l_i}{d} + \sum \zeta_i \right) \frac{u^2}{2g} = \left[0.0571 \times \left(\frac{100}{0.1} \right) + 3 \times 0.75 \right] \times \frac{0.034^2}{2 \times 9.81} = 0.0035m \quad (43)$$

Bernoulli equation gives the pump head as:

$$H_e = 10 + \frac{0.034^2}{2 \times 9.81} + \frac{9 \times 10^5}{1042 \times 9.81} + 0.0035 = 98.05m \quad (44)$$

The effective power of the pump is

$$P_e = q_v \rho g H_e = \frac{0.96}{3600} \times 1042 \times 9.81 \times 98.05 = 0.267kW \quad (45)$$

The pump shaft power is

$$P = \frac{P_e}{\eta} = \frac{0.267}{0.7} = 0.382kW \quad (46)$$

Table 2. Power requirements for microalgae slurry pump

Parameters	5 wt%	10 wt%		20 wt%	
		$\gamma = 50 \text{ s}^{-1}$	$\gamma = 100 \text{ s}^{-1}$	$\gamma = 50 \text{ s}^{-1}$	$\gamma = 100 \text{ s}^{-1}$
Viscosity (mPa·s)	1.95	1.504	1.155	1.844	1.219
Effective power (kW)	0.275	0.272	0.272	0.267	0.267
Shaft power (kW)	0.393	0.389	0.389	0.382	0.382

Table 2 summarizes the calculation results. For the above-mentioned fluid that requires high-lift delivery, a ZGB type pump can be used, which is a single-stage single-suction centrifugal slag/slurry pump. The typical processing shear rates of centrifugal pumps are within a range of 5 to 300 s^{-1} [16], which will help reduce the viscosity [17]. Because the diameter of the pipeline is 100 mm, the 100ZGB type slurry pump can be selected.

Effect of Pipe Length on Pump Power

It is assumed that the 20 wt% microalgae slurry was pumped from the storage tank to the facility. This section discusses the effect of the pipe length on the power requirement of the pump, as the length of the pipe increases to 500 meters and 1,000 meters.

When γ is 50 s^{-1} and the pipe length is 500 m, the total resistance of the pipeline is:

$$\sum H_f = \left(\lambda \frac{\sum l_i}{d} + \sum \zeta_i \right) \frac{u^2}{2g} = \left[0.0333 \times \left(\frac{500}{0.1} \right) + 3 \times 0.75 \right] \times \frac{0.034^2}{2 \times 9.81} = 0.00994m \quad (47)$$

Pump head is calculated as:

$$H_e = 10 + \frac{0.034^2}{2 \times 9.81} + \frac{9 \times 10^5}{1042 \times 9.81} + 0.00994 = 98.056m \quad (48)$$

The effective power of the pump is

$$P_e = q_v \rho g H_e = \frac{0.96}{3600} \times 1042 \times 9.81 \times 98.056 = 0.267kW \quad (49)$$

When the pipe length is 1000 m, the total resistance of the pipeline is:

$$\sum H_f = \left(\lambda \frac{\sum l_i}{d} + \sum \zeta_i \right) \frac{u^2}{2g} = \left[0.0333 \times \left(\frac{1000}{0.1} \right) + 3 \times 0.75 \right] \times \frac{0.034^2}{2 \times 9.81} = 0.0198m \quad (50)$$

Head developed is

$$H_e = 10 + \frac{0.034^2}{2 \times 9.81} + \frac{9 \times 10^5}{1042 \times 9.81} + 0.0198 = 98.066m \quad (51)$$

The effective power of the pump is

$$P_e = q_v \rho g H_e = \frac{0.96}{3600} \times 1042 \times 9.81 \times 98.066 = 0.267kW \quad (52)$$

When the pipeline length is increased to 500 meters or 1000 meters, it does not have much impact on the pump power.

Effect of Number of Elbows on Pump Power

This section discusses the effect of the numbers of elbows on the power requirement of the pump, as the numbers of elbows increases from 3 to 10. It is assumed that the 20 wt% microalgae slurry was pumped from the storage tank to the facility through 100 m pipe and elbows.

When γ is 50 s^{-1} and the number of 90° right angle elbows is 10, the total resistance of the pipeline is:

$$\sum H_f = \left(\lambda \frac{\sum l_i}{d} + \sum \zeta_i \right) \frac{u^2}{2g} = \left[0.0333 \times \left(\frac{100}{0.1} \right) + 10 \times 0.75 \right] \times \frac{0.034^2}{2 \times 9.81} = 0.0024m \quad (53)$$

Pump head is

$$H_e = 10 + \frac{0.034^2}{2 \times 9.81} + \frac{9 \times 10^5}{1042 \times 9.81} + 0.0024 = 98.049m \quad (54)$$

The effective power of the pump is

$$P_e = q_v \rho g H_e = \frac{0.96}{3600} \times 1042 \times 9.81 \times 98.049 = 0.267 \text{ kW} \quad (55)$$

When the number of 90-degree elbows is increased from 3 to 10, it does not have much impact on the pump power requirements.

CONCLUSIONS

The pump requirements for delivering the *Chlorella* slurry with 5, 10, and 20 wt% solids at 1,000 kg/h and 10 bar were calculated. The 5 wt% microalgae slurry is a Newtonian fluid with a viscosity of 1.95 mPa·s. The 10 wt% and 20 wt% microalgae slurries are non-Newtonian fluid, whose viscosity depends on the shear rate (γ). The viscosity of 10 wt% and 20 wt% microalgae slurries are 1.504 ($\gamma = 50 \text{ s}^{-1}$)/1.155 ($\gamma = 100 \text{ s}^{-1}$) and 1.844 ($\gamma = 50 \text{ s}^{-1}$)/1.219 ($\gamma = 100 \text{ s}^{-1}$) mPa·s, respectively. The pump power requirements are mainly governed by the delivery pressure. The effect of the pipe length and the number of elbows is negligible. The effective power of the pump is calculated as 0.267-0.275 kW, and the shaft power at 70% efficiency is 0.382-0.393 kW. To fulfill this duty, a ZGB type single-stage single-suction centrifugal slurry pump can be used.

ACKNOWLEDGMENTS

We are grateful for the support from the School of Chemical Engineering and Pharmacy at the Wuhan Institute of Technology.

CONFLICTS OF INTEREST

The authors declare that there is no conflict of interests regarding the publication of this paper.

REFERENCES

- [1] Barkia, I., Saari, N., and Manning, S. R. (2019). Microalgae for High-Value Products Towards Human Health and Nutrition. *Marine Drugs*, 17(5), 304. DOI: 10.3390/md17050304
- [2] Zhang, B., and Wang, Y. (2013). *Biomass Processing, Conversion and Biorefinery*, Nova Science Publishers, Inc., New York.
- [3] Davis, R., Markham, J., Kinchin, C., Grundl, N., Tan, E. C., and Humbird, D. (2016). Process design and economics for the production of algal biomass: algal biomass production in open pond systems and processing through dewatering for

- downstream conversion. National Renewable Energy Lab.(NREL), Golden, CO (United States).
- [4] Davis, R. E., Markham, J. N., Kinchin, C. M., Canter, C., Han, J., Li, Q., Coleman, A., Jones, S., Wigmosta, M., and Zhu, Y. (2018). 2017 Algae Harmonization Study: Evaluating the Potential for Future Algal Biofuel Costs, Sustainability, and Resource Assessment from Harmonized Modeling. National Renewable Energy Lab.(NREL), Golden, CO (United States).
- [5] Allnut, F. C. T., and Kessler, B. A. (2015). Harvesting and Downstream Processing—and Their Economics. In: *Biomass and Biofuels from Microalgae: Advances in Engineering and Biology*, N. R. Moheimani, *et al.*, eds., Springer International Publishing, Cham, pp: 289-310. DOI: 10.1007/978-3-319-16640-7_14
- [6] Hosseinizand, H., Sokhansanj, S., and Lim, C. J. (2018). Studying the drying mechanism of microalgae *Chlorella vulgaris* and the optimum drying temperature to preserve quality characteristics. *Drying Technology*, 36(9), 1049-1060. DOI: 10.1080/07373937.2017.1369986
- [7] Santoro, I., Nardi, M., Benincasa, C., Costanzo, P., Giordano, G., Procopio, A., and Sindona, G. (2019). Sustainable and Selective Extraction of Lipids and Bioactive Compounds from Microalgae. *Molecules (Basel, Switzerland)*, 24(23), 4347. DOI: 10.3390/molecules24234347
- [8] Yang, C., Li, R., Cui, C., Liu, S., Qiu, Q., Ding, Y., Wu, Y., and Zhang, B. (2016). Catalytic hydroprocessing of microalgae-derived biofuels: a review. *Green Chemistry*, 18(13), 3684-3699. DOI: 10.1039/c6gc01239f
- [9] Yang, C., Li, R., Qiu, Q., Yang, H., Zhang, Y., Yang, B., Wu, J., Li, B., Wang, W., Ding, Y., and Zhang, B. (2020). Pyrolytic behaviors of *Scenedesmus obliquus* over potassium fluoride on alumina. *Fuel*, 263, 116724. DOI: <https://doi.org/10.1016/j.fuel.2019.116724>
- [10] Yang, C., Li, R., Zhang, B., Qiu, Q., Wang, B., Yang, H., Ding, Y., and Wang, C. (2019). Pyrolysis of microalgae: A critical review. *Fuel Processing Technology*, 186, 53-72. DOI: <https://doi.org/10.1016/j.fuproc.2018.12.012>
- [11] Zhang, B., Wu, J., Deng, Z., Yang, C., Cui, C., and Ding, Y. (2017). A Comparison of Energy Consumption in Hydrothermal Liquefaction and Pyrolysis of Microalgae. *Trends in Renewable Energy*, 3(1), 76-85. DOI: 10.17737/tre.2017.3.1.0013
- [12] Bolhouse, A. M. (2010). Rheology of algae slurries. Master Master Thesis, University of Texas at Austin
- [13] Cagney, N., Zhang, T., Bransgrove, R., Allen, M. J., and Balabani, S. (2017). Effects of cell motility and morphology on the rheology of algae suspensions. *Journal of Applied Phycology*, 29(3), 1145-1157. DOI: 10.1007/s10811-016-1033-y
- [14] Schneider, N., Fortin, T. J., Span, R., and Gerber, M. (2016). Thermophysical properties of the marine microalgae *Nannochloropsis salina*. *Fuel Processing Technology*, 152, 390-398. DOI: <https://doi.org/10.1016/j.fuproc.2016.06.039>
- [15] Green, D. W., and Perry, R. H. (2019). *Perry's Chemical Engineers' Handbook/edición Don W. Green y Robert H. Perry*.

- [16] Wileman, A., Ozkan, A., and Berberoglu, H. (2012). Rheological properties of algae slurries for minimizing harvesting energy requirements in biofuel production. *Bioresource Technology*, 104, 432-439. DOI: <https://doi.org/10.1016/j.biortech.2011.11.027>
- [17] Mettu, S., Yao, S., Law, S. Q. K., Sun, Z., Scales, P. J., Ashokkumar, M., and Martin, G. J. O. (2019). Rheological properties of concentrated slurries of harvested, incubated and ruptured *Nannochloropsis* sp. cells. *BMC Chemical Engineering*, 1(1), 8. DOI: 10.1186/s42480-019-0011-y

Article copyright: © 2020 Jiayi Li, Yinhang Qu, Yu Gong, Changyan Yang, Bohan Yang, Peng Liu, Bo Zhang, and Yigang Ding. This is an open access article distributed under the terms of the [Creative Commons Attribution 4.0 International License](https://creativecommons.org/licenses/by/4.0/), which permits unrestricted use and distribution provided the original author and source are credited.



Management Information Systems and Data Science in the Smart Grid – Inner Class Area Capacity Distribution of the iSHM Class Maps of Overhead Low-Voltage Broadband over Power Lines Topologies

Athanasios G. Lazaropoulos^{1,2,*}

1: School of Electrical and Computer Engineering / National Technical University of Athens / 9 Iroon Polytechniou Street / Zografou, GR 15780

2: Department of Industrial Design and Production Engineering / School of Engineering / University of West Attica / 250 Thivon & P. Ralli / Athens, GR 12244

Received August 20, 2020; Accepted September 21, 2020; Published September 27, 2020

On the basis of the initial Statistical Hybrid Model (iSHM), the iSHM class maps, which are 2D contour plots and may graphically classify the real and virtual OV LV BPL topologies into five class areas, are upgraded in this paper by exploiting the third dimension of the capacity so that the upgraded class maps can provide additional information concerning the inner class area capacity distribution. The comprehension of the behavior of the inner class area capacity distribution is critical in order to deeper understand the extent and the position of iSHM class map footprints when various operation conditions of OV LV BPL topologies occur. Two inner class area capacity distribution rule of thumbs that deal with the OV LV BPL topology classification and capacity estimation are proposed thus supporting the management information system of OV LV BPL networks.

Keywords: Smart Grid; Broadband over Power Lines (BPL) networks; Power Line Communications (PLC); Distribution and Transmission Power Grids; Capacity, Statistics; Modeling; Management Information Systems; Data Science

1. Introduction

Broadband over Power Lines (BPL) technology can be considered to be one among the communications solutions, such as Radio Frequency (RF) mesh, modified Long Term Evolution (LTE), Code Division Multiple Access (CDMA) at sub GHz bands, dedicated fiber along high voltage lines and 5G communications, that is going to help towards the transformation of the existing power grid into an advanced IP-based communications network enhanced with a plethora of broadband smart grid applications [1], [2].

Since BPL technology exploits the available power grid infrastructure (*i.e.*, Multiconductor Transmission Line (MTL) configurations and related power devices), which is anyway designed to deliver power rather to support communications, high and frequency-selective channel attenuation remains as one of the critical deficiencies of the

*Corresponding author: AGLazaropoulos@gmail.com

BPL signal propagation and transmission. Among the different categories of BPL channel models, a great number of statistical BPL channel models, has been proposed in a variety of BPL technology application fields [3]-[14]. SHM that has been recently proposed in [7]-[9] is based on the Deterministic Hybrid Model (DHM), which has been exhaustively tested in transmission and distribution BPL networks [15]-[17], and is hereafter applied as the required SHM system input procedure. Actually, initial Statistical Hybrid Model (iSHM), which is one of the two supported versions of SHM and is employed in this paper, offers simulation results that are treated as the statistically processed DHM numerical results through a set of appropriate Channel Attenuation Statistical Distributions (CASDs); say, Gaussian, Lognormal, Wald, Weibull and Gumbel CASDs. Until now, the impact of a variety of parameters on the iSHM simulation results has been investigated so far such as the topology length, the interconnections between branches / main lines, branch lengths, distances between branches, branch terminations and channel attenuation measurement differences between the theoretical and practical results due to the real operation conditions [8], [18], [19]. Apart from the impact of the aforementioned intrinsic parameters, critical events during the operation of power grids, such as branch line faults and hook-style energy thefts, can be detected even if real operation conditions occur by exploiting the class maps footprints of iSHM [20], [21]; here, it should be reminded that a class map is a 2D contour plot that: (i) graphically classifies real and virtual BPL topologies in terms of their CASD Maximum Likelihood Estimator (MLE) parameter pairs and capacity; (ii) illustrates the borders between the BPL topology classes; and (iii) corresponds each CASD MLE parameter pair to its BPL topology subclass average capacity for given power grid type, CASD, coupling scheme, Injected Power Spectral Density Limits (IPSD) limits and noise Power Spectral Density (PSD) levels; while class map footprints are the graphical correspondence of CASD MLE parameter pair with the capacity that are represented on the class maps and may assess the impact of the intrinsic parameter change or the existence of critical events during the power grid operations. As the OV LV BPL topologies are examined in this paper, when changes of intrinsic parameters or the aforementioned critical events occur the respective CASD MLE parameters of the modified OV LV BPL topologies tend to change their iSHM footprint locations on the class maps following patterns of the same capacity behavior as presented in [20], [22]. In this paper, the inner class area capacity distribution of the iSHM class maps of OV LV BPL topologies is first investigated while the differences between the capacity of the aforementioned modified OV LV BPL topologies and the respective BPL topology subclass average capacities, which are used in class maps, for given CASD MLE parameter pairs is computed. On the basis of the findings of the inner class area capacity distribution of the iSHM class maps of OV LV BPL topologies and by exploiting the data science, the management information system of the BPL networks is further enhanced with two newly presented rules of thumb that allow: (i) the capacity assessment and the classification of OV LV BPL topologies by studying their CASD MLEs parameter pairs; (ii) the stability of the power grid; and (iii) the surveillance and monitoring of the power grid in order to identify possible critical events.

The rest of this short paper, which may act as a companion paper of [18], [20], [22], [23], is organized as follows: Section 2 briefly presents the theory concerning the iSHM class maps and iSHM class map footprints of OV LV BPL topologies. In Section 3, the simulation results regarding the inner class area capacity distribution are demonstrated as well as and the capacity differences between the modified OV LV BPL

topologies and the respective BPL topology subclass average capacities of iSHM class maps. The two rules of thumb concerning the monitoring and surveillance of the OV LV BPL networks are here presented.

2. iSHM Class Maps and iSHM Class Map Footprints

Prior to numerically investigate the inner class area capacity distribution in iSHM class maps, brief details concerning the definition of iSHM class maps, the iSHM class map footprints of OV LV BPL topologies and the need for this capacity distribution study of class maps are here given. Note that the values of the required operation parameters for the interconnection and the fine application of DHM, iSHM, the iSHM class maps and the iSHM class map footprints of OV LV BPL topologies are reported in [22], [23].

2.1 iSHM Class Maps

Already been mentioned, SHM consists of two versions; say, iSHM and mSHM. With reference to the BPMN diagrams of iSHM [7], [23], iSHM that is the SHM version of interest in this paper consists of six Phases. The input parameters of iSHM, which coincide with the ones of DHM, are the topological characteristics of the examined real indicative OV LV BPL topologies, the applied coupling schemes, IPSD limits and noise PSD levels while the output of iSHM is the capacity range of each OV LV BPL topology class for given CASD. Also, iSHM supports five CASDs with their corresponding MLEs (*i.e.*, Gaussian, Lognormal, Wald, Weibull and Gumbel CASDs). According to [20], each iSHM CASD exhibits different performance depending on the input parameters but Weibull CASD performs the best performance among the available ones in terms of the performance capacity metrics of the absolute threshold of percentage change and the average absolute percentage change when OV LV BPL topologies are examined. Hence, the CASD approximation accuracy to the real capacity results of [20] mandates the use of Weibull CASD for the further analysis of OV LV BPL topologies in this paper, which is anyway reevaluated for its accuracy during the critical events assumed in this paper.

To enrich the five OV LV BPL topology classes, which are straightforward defined after the initial selection of the five respective real indicative OV LV BPL topologies of Table 1 of [23], with other OV LV BPL topologies, the iSHM definition procedure, which has been proposed in [24], statistically defines virtual indicative OV LV BPL topologies by using iSHM CASD MLE parameter pairs and inserts the virtual topologies to the existing five OV LV BPL topology classes. The flowchart of the iSHM definition procedure for OV LV BPL topologies is given in Fig. 3(a) of [23]. Class maps are the output of the iSHM definition procedure where: (i) each CASD MLE parameter pair is corresponded to its OV LV BPL topology subclass average capacity; (ii) CASD MLE parameter pairs can describe real and virtual OV LV BPL topology subclasses; (iii) OV LV BPL topology class areas may be illustrated with respect to the computed capacity borders between the OV LV BPL topology classes; and (iv) with respect to the capacity borders of OV LV BPL topology classes and the Weibull CASD capacity performance, OV LV BPL topology subclasses can be arranged on the class maps by exploiting their CASD MLE parameter pairs.

2.2 iSHM Footprints on Class Maps

iSHM footprints that are added on the class maps as groups of white spots can graphically assess the impact of the intrinsic parameter changes or the existence of critical events during the power grid operation and can help towards the quick identification of the critical events for future actions by the management information system of the smart grid. The theoretical definition of iSHM footprints has been presented in [23] while a variety of applications of iSHM footprints has been presented so far, such as the iSHM footprints of the real OV LV BPL topologies, of the OV LV BPL topologies with a sole branch line fault and of the OV LV BPL topologies with a single hook for energy theft [20]. By studying iSHM footprints of OV LV BPL topologies, it is clear that the iSHM footprint extent, size, white spot positions and white spot group direction with respect to the real indicative OV LV BPL topologies may imply the intrinsic parameter change or the nature of the occurred critical events during the power grid operation.

Until now, Weibull CASD is applied during the preparation of iSHM footprints of OV LV BPL topologies due to the best performance among the available supported iSHM CASDs in terms of the performance capacity metrics of the absolute threshold of percentage change and average absolute percentage change when the indicative real OV LV BPL topologies have been assumed [20]. The goal of this paper and of the following Section is to assess the capacity estimation accuracy of iSHM footprints for given Weibull CASD MLEs that come from the OV LV BPL topologies that suffer from intrinsic parameter change or critical events, briefly denoted as modified OV LV BPL topologies, and, hence, justifies the white spot positions and directions of the respective iSHM footprints on the iSHM class maps. The aforementioned assessment can be accomplished either qualitatively by further investigating the inner class area capacity distribution of the iSHM class maps or quantitatively by comparing the capacity of the modified OV LV BPL topologies with the average capacity of the OV LV BPL topology subclass of iSHM class maps whose CASD MLE parameter pair is the same with the one of the examined modified OV LV BPL topology.

3. Numerical Results and Discussion

In this Section, numerical results that investigate the inner class area capacity distribution of the iSHM class maps of OV LV BPL topologies are first demonstrated so that a clearer image of the relation between Weibull CASD MLE parameter pair and the OV LV BPL topology subclass average capacity can be shown. This study allows the easier matching between the Weibull CASD MLEs of the examined modified OV LV BPL topologies and the capacity as defined by the iSHM class maps. Then, for the cases of: (i) arbitrary real OV LV BPL topologies; (ii) real indicative OV LV BPL topologies with arbitrary branch line faults; and (iii) real indicative OV LV BPL topologies with arbitrary hook-style energy thefts, their capacities are reported and are compared against the average capacity of the OV LV BPL topology subclass of iSHM class maps whose CASD MLE parameter pair is the same with the one of the examined modified OV LV BPL topology.

3.1 iSHM Class Maps of OV LV BPL Topologies

Already been mentioned, iSHM class maps of Weibull CASD are the basis where iSHM footprints of Weibull CASD are applied onto when the modified OV LV BPL topologies are going to be examined by the management information system of the smart grid. In accordance with [20], the iSHM class map of OV LV BPL topologies is plotted in Fig. 1(a) with respect to $\hat{\alpha}_{MLE}^{Weibull}$ and $\hat{\beta}_{MLE}^{Weibull}$ for the default operation settings of [23] when the average capacity of each OV LV BPL topology subclass is considered. Note that as the spacings of the horizontal and vertical axes are concerned, they are assumed to be equal to 50 instead of 10 of [23] so that a clearer image of the iSHM class maps and the following iSHM footprints can be examined. The respective isodynamic capacity chart of Fig. 1(a) is plotted in Fig. 1(b) without considering the borderlines between OV LV BPL topology classes.

With reference to Figs. 1(a) and 1(b), several interesting remarks can be pointed out concerning the location of the modified OV LV BPL topologies and the inner class area capacity distribution of the iSHM class maps, namely:

- By comparing Fig. 1(b) with Fig. 3(a) of [20], it is evident that the iSHM footprint of OV LV BPL topologies with one branch is clearly constrained in the rural class area while the majority of the cases examined are approximately located at the same isodynamic capacity curve with small right or left deviations. Here it should be reminded that the OV LV BPL topologies with longer branches tend to present increased values of $\hat{\alpha}_{MLE}^{Weibull}$ and $\hat{\beta}_{MLE}^{Weibull}$ and thus are located to the upper right part of the isodynamic capacity curve while a small right shift from the isodynamic capacity curve is expected since the OV LV BPL topologies with longer branches are characterized by relatively lower capacities in comparison with the real indicative OV LV BPL rural case. The opposite situation holds for the OV LV BPL topologies with one short branch. In the case of OV LV BPL topologies with two branches, similar observations can be made but for the suburban class area and for its isodynamic capacity curves.
- As the effect of branch line faults is examined and the potential of the branch line fault detection is discussed, the iSHM footprint of OV LV BPL topologies with one branch line fault is not strictly located at adjacent isodynamic capacity curves as shown by comparing Fig. 1(b) with Fig. 5 of [20]. In fact, the identification of the OV LV BPL topologies with branch line faults of short length becomes easier since their corresponding iSHM footprint violates the class area borders in accordance with [20]. The violation of the class area borders is anyway an easy task for the management information system of the smart grid to detect.

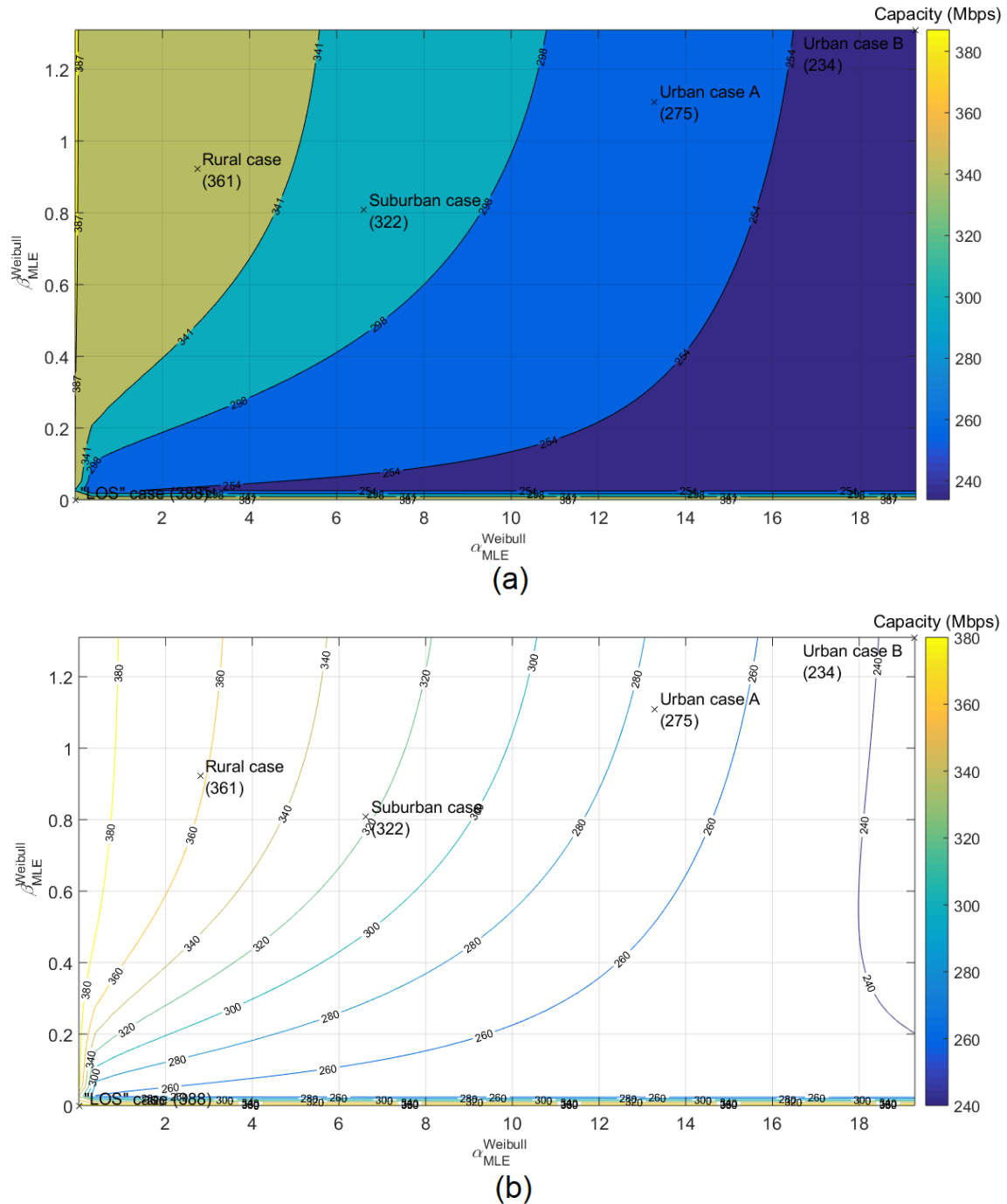


Fig. 1. (a) iSHM class map of OV LV BPL topologies when 3-30MHz frequency band, 0.1MHz frequency subchannel spacing, WtG¹ coupling scheme and FCC Part 15 are assumed [20]. (b) Isodynamic capacity chart of Fig.1(a) with isodynamic capacity curves.

The same result is reached by comparing the location of white spots of the iSHM footprint of OV LV BPL topologies with one branch line fault with the isodynamic capacity curves.

- As the effect of single hooks for energy theft is examined and their detection potential is studied, the iSHM footprint of OV LV BPL topologies with one hook

for energy theft is significantly right shifted from the real indicative OV LV BPL topology of reference. Since the vast majority of the white spots of the iSHM footprint of OV LV BPL topologies with one hook for energy theft is dislocated and approximately located on an isodynamic capacity curve far right, this implies that the detection of energy thefts is far easier by the management information system than the detection of branch line faults.

With reference to Fig. 1(b), it is clearly shown that the inner class area capacity distribution of the iSHM class maps remains zonal and solid without islands of capacity changes. The violation of isodynamic capacity curves helps towards the identification of a critical event during the operation of the power grid while the Weibull CASD MLE parameter pair can help towards the exact location of the critical event when the nature of the critical situation is identified by the management information system given the low intensity of the measurement differences.

But the aforementioned identification and classification of the critical situation presumes that the capacity of the modified OV LV BPL topology that suffers from the critical event is equal to the capacity of the applied isodynamic capacity curve which is plotted on the basis of the average capacities of the OV LV BPL topology subclass of Weibull CASD iSHM class map. For that reason, the capacity of the modified OV LV BPL topologies is compared with the average capacity of the OV LV BPL topology subclass of Weibull CASD iSHM class maps whose CASD MLE parameter pair is the same with the one of the examined modified OV LV BPL topology.

Note that the presentation of the topological characteristics of OV LV BPL topologies of the following Sections in this paper is made on the basis of the scheme of the typical OV LV BPL topology that is illustrated in Fig. 1(b) of [23]. Also, the topological characteristics of the five indicative OV LV BPL topologies, which act as the representative topologies of the respective classes and their main subclasses, are reported in Table 1 of [23] and on that basis the presentation of the topological characteristics of the arbitrary OV LV BPL topologies of the following Sections is given in the following Tables.

3.2 iSHM Footprints and Capacity Differences of the Real OV LV BPL Topologies for the Default Operation Settings

In Sec.2.4 of [20], the footprint of the real OV LV BPL topologies has been illustrated on the iSHM class maps where real OV LV BPL topologies have been retrieved by the Topology Identification Methodology (TIM) database of [25]. As the applied TIM BPL topology database specifications are concerned, they have been reported in [25] for the database preparation. For the further analysis of this Section, 12 arbitrary real OV LV BPL topologies of one branch and 16 arbitrary real OV LV BPL topologies of two branches, which are reported in Table 1 and 2, respectively, are assumed.

As the iSHM footprint parameters of the arbitrary real OV LV BPL topologies with one branch are concerned, Weibull CASD MLE parameter pairs (say, $\hat{\alpha}_{MLE}^{Weibull}$ and $\hat{\beta}_{MLE}^{Weibull}$) of each of the 12 arbitrary real OV LV BPL topologies of one branch are reported in Table 1 as well as the capacity of the examined OV LV BPL topology. Also, the average capacity of the OV LV BPL topology subclass of Weibull CASD iSHM class map for given arbitrary real OV LV BPL topology of one branch is

Table 1
Real OV LV BPL Topologies of one Branch, Weibull CASD MLEs and Capacities

Topology Number (<i>l</i>)	Length of Distribution Lines	Length of Branches	Weibull CASD MLEs		Capacity of the examined OV LV BPL Topology	Average Capacity of the Respective OV LV BPL Topology Subclass of the Weibull iSHM Class Map	Capacity Difference
			$\hat{\alpha}_{MLE}^{Weibull}$	$\hat{\beta}_{MLE}^{Weibull}$	(Mbps) C_1	(Mbps) C_2	(Mbps) $C_1 - C_2$
1.1	$L_1=10m,$ $L_2=990m$	$L_{b1}=1m$	0.188	1.071	385.938	385.936	0.002
1.2	$L_1=10m,$ $L_2=990m$	$L_{b1}=10m$	2.559	0.596	352.727	353.143	-0.416
1.3	$L_1=10m,$ $L_2=990m$	$L_{b1}=50m$	2.366	0.61	355.149	356.458	-1.308
1.4	$L_1=10m,$ $L_2=990m$	$L_{b1}=200m$	2.837	0.739	356.145	356.761	-0.616
1.5	$L_1=200m,$ $L_2=800m$	$L_{b1}=1m$	0.188	1.071	385.938	385.936	0.002
1.6	$L_1=200m,$ $L_2=800m$	$L_{b1}=10m$	2.559	0.596	352.727	353.143	-0.416
1.7	$L_1=200m,$ $L_2=800m$	$L_{b1}=50m$	2.366	0.61	355.149	356.458	-1.308
1.8	$L_1=200m,$ $L_2=800m$	$L_{b1}=200m$	2.837	0.739	356.145	356.761	-0.616
1.9	$L_1=850m,$ $L_2=150m$	$L_{b1}=1m$	0.188	1.071	385.938	385.936	0.002
1.10	$L_1=850m,$ $L_2=150m$	$L_{b1}=10m$	2.559	0.596	352.727	353.143	-0.416
1.11	$L_1=850m,$ $L_2=150m$	$L_{b1}=50m$	2.366	0.61	355.149	356.458	-1.308
1.12	$L_1=850m,$ $L_2=150m$	$L_{b1}=200m$	2.837	0.739	356.145	356.761	-0.616

Table 2
Real OV LV BPL Topologies of two Branches, Weibull CASD MLEs and Capacities

Topology Number (I)	Length of Distribution Lines	Length of Branches	Weibull CASD MLEs		Capacity of the examined OV LV BPL Topology	Average Capacity of the Respective OV LV BPL Topology Subclass of the Weibull iSHM Class Map	Capacity Difference
			$\hat{\alpha}_{MLE}^{Weibull}$	$\hat{\beta}_{MLE}^{Weibull}$	(Mbps) C_1	(Mbps) C_2	(Mbps) $C_1 - C_2$
2.1	$L_1=10m,$ $L_2=150m,$ $L_3=840m$	$L_{b1}=15m,$ $L_{b2}=3m$	9.081	0.903	304.988	303.73	1.258
2.2	$L_1=10m,$ $L_2=150m,$ $L_3=840m$	$L_{b1}=15m,$ $L_{b2}=20m$	6.888	0.83	319.504	320.204	-0.7
2.3	$L_1=10m,$ $L_2=150m,$ $L_3=840m$	$L_{b1}=50m,$ $L_{b2}=3m$	8.624	0.864	305.426	306.208	-0.782
2.4	$L_1=10m,$ $L_2=150m,$ $L_3=840m$	$L_{b1}=50m,$ $L_{b2}=20m$	6.418	0.794	321.92	323.018	-1.098
2.5	$L_1=10m,$ $L_2=300m,$ $L_3=690m$	$L_{b1}=15m,$ $L_{b2}=3m$	9.112	0.91	305.488	303.69	1.798
2.6	$L_1=10m,$ $L_2=300m,$ $L_3=690m$	$L_{b1}=15m,$ $L_{b2}=20m$	6.919	0.835	319.464	320.144	-0.68
2.7	$L_1=10m,$ $L_2=300m,$ $L_3=690m$	$L_{b1}=50m,$ $L_{b2}=3m$	8.767	0.888	304.868	305.882	-1.013
2.8	$L_1=10m,$ $L_2=300m,$ $L_3=690m$	$L_{b1}=50m,$ $L_{b2}=20m$	6.563	0.811	321.449	322.38	-0.931
2.9	$L_1=550m,$ $L_2=150m,$ $L_3=300m$	$L_{b1}=15m,$ $L_{b2}=3m$	9.081	0.903	304.988	303.73	1.258
2.10	$L_1=550m,$ $L_2=150m,$ $L_3=300m$	$L_{b1}=15m,$ $L_{b2}=20m$	6.888	0.83	319.504	320.204	-0.7
2.11	$L_1=550m,$ $L_2=150m,$ $L_3=300m$	$L_{b1}=50m,$ $L_{b2}=3m$	8.624	0.864	305.426	306.208	-0.782
2.12	$L_1=550m,$ $L_2=150m,$ $L_3=300m$	$L_{b1}=50m,$ $L_{b2}=20m$	6.418	0.794	321.92	323.018	-1.098
2.13	$L_1=550m,$ $L_2=300m,$ $L_3=150m$	$L_{b1}=15m,$ $L_{b2}=3m$	9.112	0.91	305.488	303.69	1.798
2.14	$L_1=550m,$ $L_2=300m,$ $L_3=150m$	$L_{b1}=15m,$ $L_{b2}=20m$	6.919	0.835	319.464	320.144	-0.68

2.15	$L_1=550\text{m},$ $L_2=300\text{m},$ $L_3=150\text{m}$	$L_{b1}=50\text{m},$ $L_{b2}=3\text{m}$	8.767	0.888	304.868	305.882	-1.013
2.16	$L_1=550\text{m},$ $L_2=300\text{m},$ $L_3=150\text{m}$	$L_{b1}=50\text{m},$ $L_{b2}=20\text{m}$	6.563	0.811	321.449	322.38	-0.931

demonstrated as well as the capacity difference between the examined OV LV BPL topology and the average capacity of the OV LV BPL topology subclass of Weibull CASD iSHM class map of the same Weibull CASD MLE parameter pair with the one of the examined OV LV BPL topology. In Table 2, the same analytics with Table 1 are shown but for the case of the 16 arbitrary real OV LV BPL topologies of two branches.

By analyzing Tables 1 and 2, several important observations can be made concerning the iSHM footprints of the real OV LV BPL topologies and the inner class area capacity distribution of the iSHM class maps, namely:

- With reference to Weibull CASD MLEs, all the arbitrary OV LV BPL topologies of Table 1 and 2 are located at the rural and suburban class areas, respectively. This quantitative observation agrees with the graphical findings of iSHM footprints highlighted at Figs. 3(a) and 3(b) of [20].
- In Table 1, all the capacities of the arbitrary OV LV BPL topologies of one branch remain comparable except for Topologies 1.1, 1.5 and 1.9, which are characterized by the short branches of 1m. The almost equal capacities of the aforementioned arbitrary OV LV BPL topologies imply that their iSHM footprint lies near the same isodynamic capacity curve of 355Mbps. Same capacity results occur in Table 2 where the arbitrary OV LV BPL topologies of two branches are grouped to three isodynamic capacity curves.
- In accordance with Table 2 of [20], Weibull CASD succeeds in satisfying the strict capacity performance criteria of absolute threshold of percentage change and average absolute percentage change for the five indicative OV LV BPL topologies. In Table 1, it is shown that the capacity of the examined arbitrary OV LV BPL topology with one branch is approximately the same with the average capacity of the respective OV LV BPL topology subclass of the Weibull iSHM class map of Fig. 1(a) (say, capacity differences that range from -1.308Mbps to 0.002Mbps) that entails that Weibull CASD can accurately approximate the capacity of each OV LV BPL topology of one branch given the Weibull CASD MLEs. Same results can be observed in the case of OV LV BPL topologies with two branches where the capacity differences range from -1.098Mbps to 1.798Mbps. Therefore, Weibull CASD can produce successful capacity estimations for any OV LV BPL topology that lies at the rural and suburban class area given the Weibull CASD MLEs.

It is evident from the analysis of this Section that a direct correspondence can be assumed between Weibull CASD MLEs of an examined OV LV BPL topology, its position on the class map, its position on the isodynamic capacity curves and its capacity. Combined with the zonal capacity distribution behavior of class maps, it is shown that OV LV BPL topologies with one, two and three and above branches are expected to be located at rural, suburban and urban class areas, respectively.

3.3 iSHM Footprints and Capacity Differences of the Real OV LV BPL Topologies with One Branch Line Fault for the Default Operation Settings

In Sec.2.5 of [20], the footprint of the real OV LV BPL topologies with one branch line fault has been illustrated on the iSHM class maps where the real indicative OV LV BPL urban case A has acted as the reference topology. Actually, Fault and Instability Identification Methodology (FIIM) database of [25] has been exploited so that all the possible real OV LV BPL topologies with one branch line fault can be retrieved by the real indicative OV LV BPL urban case A. For the further analysis of this Section, 6 arbitrary real OV LV BPL topologies of one branch line fault, which are based on the topological characteristics of the real indicative OV LV BPL urban case A, are reported in Table 3. Note that two different branch line fault lengths are assumed per each of the three branch lines of the real indicative urban case A.

As the iSHM footprint parameters of the arbitrary real OV LV BPL topologies with one branch line fault are concerned, Weibull CASD MLE parameter pair of each of the 6 arbitrary real OV LV BPL topologies of one branch line fault is reported in Table 3 as well as the capacity of the examined OV LV BPL topology. Similarly to Tables 1 and 2, the average capacity of the OV LV BPL topology subclass of Weibull CASD iSHM class map for given arbitrary real OV LV BPL topology of one branch line fault and the capacity difference between the examined OV LV BPL topology and the average capacity of the OV LV BPL topology subclass of Weibull CASD iSHM class map of the same Weibull CASD MLE parameter pair with the one of the examined OV LV BPL topology are also given.

With respect to Figs. 1(a), 1(b) and Fig. 5 of [20], Table 3 may offer valuable information towards the detection of the critical event of branch line faults during the operation of the power grid by exploiting the iSHM footprints of the real OV LV BPL topologies and the inner class area capacity distribution of the iSHM class maps. More specifically:

- Similarly to Tables 1 and 2, the capacities of the examined arbitrary OV LV BPL topologies with one branch line fault remain approximately the same with the average capacities of the respective OV LV BPL topology subclasses of the Weibull iSHM class map of Fig. 1(a) (say, capacity differences that range from -3.604Mbps to 1.959Mbps). The capacity differences are small enough in comparison with the achieved capacities of the examined OV LV BPL topologies that again entails that Weibull CASD can accurately approximate the capacity of each OV LV BPL topology of one branch line fault given its Weibull CASD MLEs.
- Since a direct correspondence between the Weibull CASD MLE parameter pair and the capacity of an examined OV LV BPL topology with one branch line fault is verified, there is no need for depicting the Weibull CASD MLE parameter pair of the examined OV LV BPL topology on the class map since a simple check of the achieved capacity of the examined OV LV BPL topology by the management information system with the capacity borderlines of a class area can assure if its location lies inside the class area or not.

Table 3
OV LV BPL Urban Case A with one Branch Line Fault, Weibull CASD MLEs and Capacities

Topology Number (I)	Length of Distribution Lines	Length of Branches	Weibull CASD MLEs		Capacity of the examined OV LV BPL Topology	Average Capacity of the Respective OV LV BPL Topology Subclass of the Weibull iSHM Class Map	Capacity Difference
			$\hat{\alpha}_{MLE}^{Weibull}$	$\hat{\beta}_{MLE}^{Weibull}$	(Mbps) C_1	(Mbps) C_2	(Mbps) $C_1 - C_2$
3.1	$L_1=500m,$ $L_2=200m,$ $L_3=100m,$ $L_4=200m$	$L_{b1}=3m,$ $L_{b2}=13m,$ $L_{b3}=10m$	14.446	1.127	264.515	266.916	-2.401
3.2	$L_1=500m,$ $L_2=200m,$ $L_3=100m,$ $L_4=200m$	$L_{b1}=5m,$ $L_{b2}=13m,$ $L_{b3}=10m$	13.038	1.272	280.149	279.677	0.472
3.3	$L_1=500m,$ $L_2=200m,$ $L_3=100m,$ $L_4=200m$	$L_{b1}=8m,$ $L_{b2}=3m,$ $L_{b3}=10m$	14.423	1.045	262.214	265.818	-3.604
3.4	$L_1=500m,$ $L_2=200m,$ $L_3=100m,$ $L_4=200m$	$L_{b1}=8m,$ $L_{b2}=8m,$ $L_{b3}=10m$	11.446	0.796	279.445	281.260	-1.814
3.5	$L_1=500m,$ $L_2=200m,$ $L_3=100m,$ $L_4=200m$	$L_{b1}=8m,$ $L_{b2}=13m,$ $L_{b3}=2m$	9.993	0.987	299.801	298.681	1.120
3.6	$L_1=500m,$ $L_2=200m,$ $L_3=100m,$ $L_4=200m$	$L_{b1}=8m,$ $L_{b2}=13m,$ $L_{b3}=4m$	14.737	1.255	268.326	266.367	1.959

- Since the real indicative OV LV BPL urban case A acts as the basis for the study of single branch line faults of this Section, the capacities of the class area capacity borderlines are equal to 254Mbps and 298Mbps. By examining the Table 3, it is evident that Topology 3.5 presents capacity that is equal to 299.801Mbps and exceeds the upper capacity borderline of the urban case A class area. If a branch line fault is suspected during the operation of the power grid, this exceedance may be an alert for the management information system. Indeed, the capacity borderline violation remains the safest way to detect a potential branch line faults as also explained and depicted in Fig. 5 of [20].
- In accordance with Table 1 of [20] and Fig. 1(a), the real indicative OV LV BPL urban case A is characterized by $\hat{\alpha}_{MLE}^{Weibull}$, $\hat{\beta}_{MLE}^{Weibull}$ and capacity that are equal to 13.29, 1.11 and 275Mbps, respectively. As the OV LV BPL topologies of Table 3 are regarded, their $\hat{\alpha}_{MLE}^{Weibull}$ and $\hat{\beta}_{MLE}^{Weibull}$ range from 9.993 to 14.737 and from

0.796 to 1.272, respectively, while their capacities range from 266.367Mbps to 298.681Mbps. Since branch line fault reforms the existing affected branch line of the OV LV BPL topology to a shorter one, capacity fluctuations can be observed while a movement across the isodynamic capacity curve is expected due to the fluctuations of $\hat{\alpha}_{MLE}^{Weibull}$ and $\hat{\beta}_{MLE}^{Weibull}$.

As the violation of class area capacity borderlines and of the isodynamic capacity curves is an evidence for the existence of a branch line fault when no measurement differences are assumed, FIIM, which is analyzed in [25], can be then activated so that the branch line fault can securely identified through its supported repertory of faults and instabilities. Anyway, FIIM is a part of the management information system of the smart grid and here its performance is enhanced. As already been identified, the detection of branch line fault of short length becomes an easier task since violation of the capacity borderlines of the corresponding class area is more expected.

3.4 iSHM Footprints and Capacity Differences of the Real OV LV BPL Topologies with One Hook for Energy Theft for the Default Operation Settings

In Sec. 2.6 of [20], the footprint of the real OV LV BPL topologies with a single hook for energy theft has been shown on the iSHM class maps where the real indicative OV LV BPL suburban case has acted as the basis topology. In accordance to [26], Hook Style energy theft DETection (HS-DET) method may generate all the real OV LV BPL topologies with a single hook for energy theft that are based on the OV LV BPL suburban case but for the sake of the analysis of this Section, 9 arbitrary real OV LV BPL topologies of one hook for energy theft, which are based on the topological characteristics of the real indicative OV LV BPL suburban case, are reported in Table 4.

As the iSHM footprint parameters of the arbitrary real OV LV BPL topologies with one hook for energy theft are concerned, Weibull CASD MLE parameter pair of each of the 9 arbitrary real OV LV BPL topologies of one hook for energy theft is reported in Table 4 as well as the capacity of the examined OV LV BPL topology. Similarly to Tables 1-3, the average capacity of the OV LV BPL topology subclass of Weibull CASD iSHM class map for given arbitrary real OV LV BPL topology of one hook for energy theft and the capacity difference between the examined OV LV BPL topology and the average capacity of the OV LV BPL topology subclass of Weibull CASD iSHM class map of the same Weibull CASD MLE parameter pair with the one of the examined OV LV BPL topology are also given.

Table 4
 OV LV BPL Suburban Case with one Single Hook for Energy Theft, Weibull CASD MLEs and Capacities

Topology Number (I)	Length of Distribution Lines	Length of Branches	Weibull CASD MLEs		Capacity of the examined OV LV BPL Topology	Average Capacity of the Respective OV LV BPL Topology Subclass of the Weibull iSHM Class Map	Capacity Difference
			$\hat{\alpha}_{MLE}^{Weibull}$	$\hat{\beta}_{MLE}^{Weibull}$	(Mbps) C_1	(Mbps) C_2	(Mbps) $C_1 - C_2$
4.1	$L_1=1m,$ $L_2=499m,$ $L_3=400m,$ $L_4=100m$	$L_{b1}=3m,$ $L_{b2}=50m,$ $L_{b3}=10m$	13.564	1.057	272.983	272.305	0.678
4.2	$L_1=1m,$ $L_2=499m,$ $L_3=400m,$ $L_4=100m$	$L_{b1}=15m,$ $L_{b2}=50m,$ $L_{b3}=10m$	11.463	1.006	287.521	287.316	0.205
4.3	$L_1=1m,$ $L_2=499m,$ $L_3=400m,$ $L_4=100m$	$L_{b1}=100m,$ $L_{b2}=50m,$ $L_{b3}=10m$	11.196	1.078	291.723	291.085	0.638
4.4	$L_1=200m,$ $L_2=300m,$ $L_3=400m,$ $L_4=100m$	$L_{b1}=3m,$ $L_{b2}=50m,$ $L_{b3}=10m$	13.501	1.069	273.302	272.997	0.305
4.5	$L_1=200m,$ $L_2=300m,$ $L_3=400m,$ $L_4=100m$	$L_{b1}=15m,$ $L_{b2}=50m,$ $L_{b3}=10m$	11.289	0.998	288.358	288.498	-0.140
4.6	$L_1=200m,$ $L_2=300m,$ $L_3=400m,$ $L_4=100m$	$L_{b1}=100m,$ $L_{b2}=50m,$ $L_{b3}=10m$	11.053	1.057	292.244	291.770	0.474
4.7	$L_1=500m,$ $L_2=200m,$ $L_3=200m,$ $L_4=100m$	$L_{b1}=50m,$ $L_{b2}=3m,$ $L_{b3}=10m$	13.438	1.044	272.895	272.996	-0.102
4.8	$L_1=500m,$ $L_2=200m,$ $L_3=200m,$ $L_4=100m$	$L_{b1}=50m,$ $L_{b2}=15m,$ $L_{b3}=10m$	11.271	0.977	287.904	288.103	-0.199
4.9	$L_1=500m,$ $L_2=200m,$ $L_3=200m,$ $L_4=100m$	$L_{b1}=50m,$ $L_{b2}=100m,$ $L_{b3}=10m$	11.170	1.092	292.164	291.580	0.585

With respect to Figs. 1(a), 1(b) and Fig. 7 of [20], Table 4 verifies the convenience to detect the energy theft by the management information system of the smart grid. Since the hook of energy theft may be treated as an additional branch line to the existing ones of the examined OV LV BPL topology, this implies the transition of the examined OV LV BPL topology from the existing topology class to the one more aggravated; say, in the case of this Section, the original OV LV BPL topology is located at the suburban class area while the modified ones after the insertion of hook (*i.e.*, Topologies 4.1-4.9) are located at the class area of the urban case A. By taking into account the capacity of the modified OV LV BPL topologies, the low capacity differences and the capacity borderlines of the urban case A class area, it is evident that a steep decrease of the capacity that occurs due to the insertion of the hook means a possible energy theft if all other critical events are eliminated. Another iSHM footprint characteristic that has been highlighted in Table 4 is the steep and steady increase of $\hat{a}_{MLE}^{Weibull}$ with respect to $\hat{a}_{MLE}^{Weibull}$ of OV LV BPL suburban case, which is equal to 6.62 as reported in Table 1 of [20]. Also an increase of $\hat{\beta}_{MLE}^{Weibull}$ can also be observed in modified OV LV BPL topologies but this occurs in the majority of the cases as presented in Fig.7 of [20]. Due to the generalized differentiation of $\hat{a}_{MLE}^{Weibull}$, $\hat{\beta}_{MLE}^{Weibull}$ and capacity, the detection of the hook style energy theft remains easier than the one of branch line fault while the application of HS-DET method as analyzed in [26] may allow the location determination of any hook style energy theft in OV LV BPL networks.

3.5 Weibull iSHM Class Maps and Inner Class Area Capacity Distribution Rules of Thumb

As already been mentioned for Figs. 1(a) and 1(b), first, either Weibull iSHM topology class borderlines or isodynamic capacity curves create solid capacity zones without capacity islands on them. Second, it has been proven in Tables 1-4 that the capacity of the examined OV LV BPL topologies remains almost equal to the average capacity of the respective OV LV BPL topology subclasses of Weibull CASD iSHM class map for given Weibull CASD MLE parameter pair. Third, either Weibull iSHM topology class borderlines or isodynamic capacity curves can be satisfactorily approximated by equations that involve $\hat{a}_{MLE}^{Weibull}$ and $\hat{\beta}_{MLE}^{Weibull}$ thus clearly defining the limits so that (i) the examined OV LV BPL topology can be grouped among the available topology classes through its Weibull CASD MLE parameter pair; and (ii) the capacity of the examined OV LV BPL topology can be estimated through its Weibull CASD MLE parameter pair. For clarity issues, the following approximation analysis is focused: (i) between the $\hat{a}_{MLE}^{Weibull}$ and $\hat{\beta}_{MLE}^{Weibull}$ graphical limits of Figs. 1(a)-(b); and (ii) the between the $\hat{a}_{MLE}^{Weibull}$ and $\hat{\beta}_{MLE}^{Weibull}$ limits where topology class borderlines and isodynamic capacity curves remain smooth without breaks; say, $\hat{a}_{MLE}^{Weibull}$ ranges from 2 to 20 and $\hat{\beta}_{MLE}^{Weibull}$ ranges from 0.2 to 1.2.

More specifically, let assume that Weibull iSHM topology class borderlines of Fig. 1(a) and Weibull iSHM isodynamic capacity curves of Fig. 1(b) may be approximated through quadratic regression equations that are detailed in Tables 5 and 6, respectively. Now, let assume arbitrary OV LV BPL topologies, say, Topologies 1.1, 2.1, 3.1 and 4.1, whose $\hat{a}_{MLE}^{Weibull}$ and $\hat{\beta}_{MLE}^{Weibull}$ are already reported in Tables 1-4, respectively.

Table 5
Quadratic Regression Equations of iSHM Topology Class Borderlines of Fig. 1(a)

OV LV BPL Topology Class (Capacity of the Right Borderline in Mbps)	Right Borderline Equation
Rural (341)	$R_{5.1} = \hat{\beta}_{MLE}^{Weibull} - \left\{ \left[0.0236 \cdot (\hat{a}_{MLE}^{Weibull})^2 \right] + \left[0.0304 \cdot \hat{a}_{MLE}^{Weibull} \right] + 0.2174 \right\}$
Suburban (298)	$R_{5.2} = \hat{\beta}_{MLE}^{Weibull} - \left\{ \left[0.0133 \cdot (\hat{a}_{MLE}^{Weibull})^2 \right] + \left[-0.05 \cdot \hat{a}_{MLE}^{Weibull} \right] + 0.1943 \right\}$
Urban Case A (254)	$R_{5.3} = \hat{\beta}_{MLE}^{Weibull} - \left\{ \left[0.0089 \cdot (\hat{a}_{MLE}^{Weibull})^2 \right] + \left[-0.1116 \cdot \hat{a}_{MLE}^{Weibull} \right] + 0.3324 \right\}$

Table 6
Quadratic Regression Equations of iSHM isodynamic capacity curves of Fig. 1(b)

Capacity in Mbps of the Isodynamic Curve	Isodynamic Capacity Curve Equation
360	$R_{6.1} = \hat{\beta}_{MLE}^{Weibull} - \left\{ \left[0.1228 \cdot (\hat{a}_{MLE}^{Weibull})^2 \right] + \left[-0.1581 \cdot \hat{a}_{MLE}^{Weibull} \right] + 0.3878 \right\}$
340	$R_{6.2} = \hat{\beta}_{MLE}^{Weibull} - \left\{ \left[0.0391 \cdot (\hat{a}_{MLE}^{Weibull})^2 \right] + \left[-0.0703 \cdot \hat{a}_{MLE}^{Weibull} \right] + 0.3144 \right\}$
320	$R_{6.3} = \hat{\beta}_{MLE}^{Weibull} - \left\{ \left[0.0198 \cdot (\hat{a}_{MLE}^{Weibull})^2 \right] + \left[-0.0387 \cdot \hat{a}_{MLE}^{Weibull} \right] + 0.2319 \right\}$
300	$R_{6.4} = \hat{\beta}_{MLE}^{Weibull} - \left\{ \left[0.0141 \cdot (\hat{a}_{MLE}^{Weibull})^2 \right] + \left[-0.0608 \cdot \hat{a}_{MLE}^{Weibull} \right] + 0.2419 \right\}$
280	$R_{6.5} = \hat{\beta}_{MLE}^{Weibull} - \left\{ \left[0.0112 \cdot (\hat{a}_{MLE}^{Weibull})^2 \right] + \left[-0.0696 \cdot \hat{a}_{MLE}^{Weibull} \right] + 0.1897 \right\}$
260	$R_{6.6} = \hat{\beta}_{MLE}^{Weibull} - \left\{ \left[0.0081 \cdot (\hat{a}_{MLE}^{Weibull})^2 \right] + \left[-0.0715 \cdot \hat{a}_{MLE}^{Weibull} \right] + 0.1553 \right\}$

Table 7
OV LV BPL Topologies and Quadratic Regression Equations of iSHM Topology Class Borderlines of Table 5

Topology Number (<i>l</i>)	Weibull CASD MLEs		Capacity of the examined OV LV BPL Topology (Mbps)	iSHM Topology Class Right Borderline Equation		
	$\hat{a}_{MLE}^{Weibull}$	$\hat{\beta}_{MLE}^{Weibull}$		C_1	$R_{5.1}$ (Rural / 341)	$R_{5.2}$ (Suburban / 298)
1.1	0.188	1.071	385.938	0.847051	0.88563	0.759266
2.1	9.081	0.903	304.988	-1.53663	0.065971	0.850105
3.1	14.446	1.127	264.515	-4.45457	-1.12054	0.54946
4.1	13.564	1.057	272.983	-3.91472	-0.90606	0.600902

Table 8
 OV LV BPL Topologies and Quadratic Regression Equations of iSHM Isodynamic Capacity Curves of
 Table 6

Topology Number (<i>I</i>)	Weibull CASD MLEs		Capacity of the examined OV LV BPL Topology (Mbps)	iSHM Isodynamic Capacity Curve Equation					
	$\hat{\alpha}_{MLE}^{Weibull}$	$\hat{\beta}_{MLE}^{Weibull}$		C_1	$R_{6.1}$ (360)	$R_{6.2}$ (340)	$R_{6.3}$ (320)	$R_{6.4}$ (300)	$R_{6.5}$ (280)
1.1	0.188	1.071	385.938	0.649783	0.636234	0.630976	1.014192	0.637089	0.637556
2.1	9.081	0.903	304.988	-8.23454	-2.12957	-0.82496	0.109542	0.164835	0.437729
3.1	14.446	1.127	264.515	-22.6624	-6.4637	-2.89254	-2.01022	-0.65145	0.022925
4.1	13.564	1.057	272.983	-19.8381	-5.62975	-2.50752	-1.49095	-0.50615	0.089971

On the basis of $\hat{\alpha}_{MLE}^{Weibull}$ and $\hat{\beta}_{MLE}^{Weibull}$ of each of the aforementioned four topologies, the computation results of the application of iSHM topology class right borderline quadratic regression equations $R_{5.1}-R_{5.3}$ are demonstrated in Table 7 as well as the capacity of each OV LV BPL topology. Similar results with Table 7 are given in Table 8 but for the case of iSHM isodynamic capacity curve quadratic regression equations $R_{6.1}-R_{6.6}$.

By observing Tables 7 and 8, two rules of thumb that are based on the inner class area capacity distribution are first presented in the following analysis. In order to define these rules of thumb, an evidence that is very useful during the following analysis is the last positive value of quadratic regression equation results per each row (*i.e.*, per each examined OV LV BPL topology) from right to left that is filled with green color in Tables 7 and 8. As for the two rules of thumb that are proposed, the first one has to do with the classification of OV LV BPL topologies while the second one has to do with the approximate computation of the OV LV BPL topology capacity, namely:

- *First rule of thumb concerning the OV LV BPL topology classification:* As the inner class area capacity distribution suggests, the class areas are solid and are bounded by borderlines approximated by the equations of Table 5. In accordance with Table 7, the positive values for given OV LV BPL topology imply that the respective quadratic regression equations lie below the Weibull CASD MLEs of the examined OV LV BPL topology. The opposite fact holds when negative values occur. Since quadratic regression equations of Table 7 describe the right borderlines of the class areas and, hence, the respective lower capacity bounds of the class areas, the last positive value per row in Table 7 determines the OV LV BPL topology class of the examined topology. Therefore, Topology 1.1, 2.1, 3.1 and 4.1 are members of the rural, suburban, urban case A and urban case A OV LV BPL topology classes, respectively. The last remark is easily verified by comparing the capacity of the examined topology with the capacities of right borderlines of the OV LV BPL topology classes that are reported in Table 7; e.g., Topology 1.1 capacity is equal to 385.938Mbps that is greater than the lower

capacity bound of rural class, which is equal to 341Mbps, and lower than the “LOS” class capacity of 387Mbps, which is presented in Fig. 1(a) and only consists of the “LOS” case. Same observations stand for the Topologies 2.1, 3.1 and 4.1 as well as for the vast majority of the OV LV BPL topologies described by Weibull CASD MLEs.

- *Second rule of thumb concerning the capacity approximation of OV LV BPL topology:* Similarly to the first rule of thumb, isodynamic capacity curves bound compact capacity areas while the equations of the iSHM isodynamic capacity curves are given in Table 6. In accordance with Table 8, the positive values for given OV LV BPL topology imply that the respective quadratic regression equations lie below the Weibull CASD MLEs of the examined OV LV BPL topology while the negative values imply that the respective quadratic regression equations lie above. Similarly to the first rule of thumb, the last positive value per row in Table 8 may approximate the OV LV BPL topology capacity with lower and upper capacity bounds the capacity of the current isodynamic capacity curve of the last positive value and the capacity of the next isodynamic capacity curve, respectively. The last approximation is easily verified by comparing the capacity of the examined topology with the capacities of the isodynamic capacity curves that are reported in Table 8; e.g., Topology 2.1 capacity is equal to 304.988Mbps that is greater than the lower capacity bound defined by the isodynamic capacity curve $R_{6,4}$, which is equal to 300Mbps, and lower than the upper capacity bound defined by the isodynamic capacity curve $R_{6,3}$, which is equal to 320Mbps. Same observations stand for the Topologies 1.1, 3.1 and 4.1 as well as for the vast majority of the OV LV BPL topologies characterized by Weibull CASD MLEs.

4. Conclusions

In this paper, the study of the inner class area capacity distribution of Weibull iSHM class maps has allowed the better understanding of the relation between Weibull CASD MLEs and the capacity of the OV LV BPL topologies. Actually, regardless of the operation conditions of the OV LV power grid (either normal operation or faulty operation), Weibull CASD MLEs permit the capacity estimation of the examined OV LV BPL topologies. By exploiting the solid capacity areas of the Weibull iSHM class maps and iSHM footprints of the OV LV BPL topologies during their fault operation, critical events such as the branch line faults and the energy thefts can be easily detected through the careful consideration of iSHM footprints of the modified OV LV BPL topologies by the management information system of the OV LV BPL networks. Going one step further, two rules of thumb have been proposed that allow the classification and the capacity approximation of the OV LV BPL topologies by exploiting class area borderline and isodynamic capacity curve quadratic regression equations, respectively.

CONFLICTS OF INTEREST

The author declares that there is no conflict of interests regarding the publication of this paper.

References

- [1] Y. J. A. Zhang, H. P. Schwefel, H. Mohsenian-Rad, C. Wietfeld, C. Chen, and H. Gharavi, "Guest Editorial Special Issue on Communications and Data Analytics in Smart Grid," *IEEE Journal on Selected Areas in Communications*, vol. 38, no. 1, pp. 1-4, 2020.
- [2] A. G. Lazaropoulos, "Wireless Sensor Network Design for Transmission Line Monitoring, Metering and Controlling Introducing Broadband over PowerLines-enhanced Network Model (BPLeNM)," *ISRN Power Engineering*, vol. 2014, Article ID 894628, 22 pages, 2014. doi:10.1155/2014/894628. [Online]. Available: <http://www.hindawi.com/journals/isrn.power.engineering/2014/894628/>
- [3] A. M. Tonello and T. Zheng, "Bottom-up transfer function generator for broadband PLC statistical channel modeling," In *Proc. IEEE International Symposium on Power Line Communications and Its Applications 2009, ISPLC 2009*, pp. 7-12, Mar. 2009.
- [4] A. M. Tonello and F. Versolatto, "Bottom-up statistical PLC channel modeling—Part I: Random topology model and efficient transfer function computation," *IEEE Transactions on Power Delivery*, vol. 26, no. 2, pp. 891-898, 2011.
- [5] A. Pittolo and A. M. Tonello, "A synthetic statistical mimo plc channel model applied to an in-home scenario," *IEEE Trans. on Commun.*, vol. 65, no. 6, pp. 2543-2553, 2017.
- [6] A. M. Tonello and F. Versolatto, "Bottom-up statistical PLC channel modeling—Part II: Inferring the statistics," *IEEE Trans. on Power Del.*, vol. 25, no. 4, pp. 2356-2363, 2010.
- [7] A. G. Lazaropoulos, "Statistical Broadband over Power Lines Channel Modeling – Part 1: The Theory of the Statistical Hybrid Model," *Progress in Electromagnetics Research C*, vol. 92, pp. 1-16, 2019. [Online]. Available: <http://www.jpier.org/PIERC/pierc92/01.19012902.pdf>
- [8] A. G. Lazaropoulos, "Statistical Broadband over Power Lines (BPL) Channel Modeling – Part 2: The Numerical Results of the Statistical Hybrid Model," *Progress in Electromagnetics Research C*, vol. 92, pp. 17-30, 2019. [Online]. Available: <http://www.jpier.org/PIERC/pierc92/02.19012903.pdf>
- [9] A. G. Lazaropoulos, "Enhancing the Statistical Hybrid Model Performance in Overhead and Underground Medium Voltage Broadband over Power Lines Channels by Adopting Empirical Channel Attenuation Statistical Distribution," *Trends in Renewable Energy*, vol. 5, no. 2, pp. 181-217, 2019. [Online]. Available: <http://futureenergysp.com/index.php/tre/article/view/96/pdf>
- [10] T. Oliveira, A. Picorone, C. Zeller, S. Netto, and M. Ribeiro, "Statistical Modeling of Brazilian In-Home PLC Channel Features," *Journal of Communication and Information Systems*, vol. 34, no. 1, pp. 154-168, 2019.

- [11] T. R. Oliveira, C. B. Zeller, S. L. Netto, and M. V. Ribeiro, "Statistical modeling of the average channel gain and delay spread in in-home PLC channels," in *Proc. in IEEE International Symposium on Power Line Communications and Its Applications*, pp. 184-188, Austin, TX, USA Mar. 2015.
- [12] J. A. Cortes, F. J. Canete, L. Diez, and J. L. G. Moreno, "On the statistical properties of indoor power line channels: Measurements and models," in *Proc. IEEE International Symposium on Power Line Communications and Its Applications*, pp. 271-276, Apr. 2011.
- [13] A. M. Tonello, F. Versolatto, and A. Pittolo, "In-home power line communication channel: Statistical characterization," *IEEE Trans. on Commun.*, vol. 62, no. 6, pp. 2096–2106, Jun. 2014.
- [14] S. Galli, "A novel approach to the statistical modeling of wireline channels," *IEEE Trans. on Commun.*, vol. 59, no. 5, pp. 1332–1345, May 2011.
- [15] A. G. Lazaropoulos and P. G. Cottis, "Transmission characteristics of overhead medium voltage power line communication channels," *IEEE Trans. Power Del.*, vol. 24, no. 3, pp. 1164-1173, Jul. 2009.
- [16] A. G. Lazaropoulos and P. G. Cottis, "Broadband transmission via underground medium-voltage power lines-Part I: transmission characteristics," *IEEE Trans. Power Del.*, vol. 25, no. 4, pp. 2414-2424, Oct. 2010.
- [17] A. G. Lazaropoulos, "Towards Modal Integration of Overhead and Underground Low-Voltage and Medium-Voltage Power Line Communication Channels in the Smart Grid Landscape: Model Expansion, Broadband Signal Transmission Characteristics, and Statistical Performance Metrics (Invited Paper)," *ISRN Signal Processing*, vol. 2012, Article ID 121628, pp. 1-17, 2012. [Online]. Available: <http://www.hindawi.com/isrn/sp/2012/121628/>
- [18] A. G. Lazaropoulos, "Virtual Indicative Broadband over Power Lines Topologies for Respective Subclasses by Adjusting Channel Attenuation Statistical Distribution Parameters of Statistical Hybrid Models – Part 2: Numerical Results for the Overhead and Underground Medium-Voltage Power Grids," *Trends in Renewable Energy*, vol. 5, no. 3, pp. 258-281, Aug. 2019. [Online]. Available: <http://futureenergysp.com/index.php/tre/article/view/100/pdf>
- [19] A. G. Lazaropoulos, "Business Analytics and IT in Smart Grid – Part 2: The Qualitative Mitigation Impact of Piecewise Monotonic Data Approximations on the iSHM Class Map Footprints of Overhead Low-Voltage Broadband over Power Lines Topologies Contaminated by Measurement Differences," *Trends in Renewable Energy*, vol. 6, no. 2, pp. 187-213, 2020. [Online]. Available: <http://futureenergysp.com/index.php/tre/article/download/118/94>
- [20] A. G. Lazaropoulos, "Statistical Channel Modeling of Overhead Low Voltage Broadband over Power Lines (OV LV BPL) Networks – Part 2: The Numerical Results of Class Map Footprints of Real OV LV BPL Topologies, Branch Line Faults and Hook Style Energy Thefts," *Trends in Renewable Energy*, vol. 6, no. 1, pp. 88-109, Mar. 2020. [Online]. Available: <http://futureenergysp.com/index.php/tre/article/download/113/pdf>
- [21] I. C. Demetriou and M. J. D. Powell, "Least squares smoothing of univariate data to achieve piecewise monotonicity," *IMA Journal of Numerical Analysis*, vol. 11, no. 3, pp. 411-432, 1991.
- [22] A. G. Lazaropoulos, "Business Analytics and IT in Smart Grid – Part 1: The Impact of Measurement Differences on the iSHM Class Map Footprints of

- Overhead Low-Voltage Broadband over Power Lines Topologies,” *Trends in Renewable Energy*, vol. 6, no. 2, pp. 156-186, 2020. [Online]. Available: <http://futureenergysp.com/index.php/tre/article/download/117/93>
- [23] A. G. Lazaropoulos, “Statistical Channel Modeling of Overhead Low Voltage Broadband over Power Lines (OV LV BPL) Networks – Part 1: The Theory of Class Map Footprints of Real OV LV BPL Topologies, Branch Line Faults and Hook-Style Energy Thefts,” *Trends in Renewable Energy*, vol. 6, no. 1, pp. 61-87, Mar. 2020. [Online]. Available: <http://futureenergysp.com/index.php/tre/article/download/112/pdf>
- [24] A. G. Lazaropoulos, “Virtual Indicative Broadband over Power Lines Topologies for Respective Subclasses by Adjusting Channel Attenuation Statistical Distribution Parameters of Statistical Hybrid Models – Part 1: Theory,” *Trends in Renewable Energy*, vol. 5, no. 3, pp. 237-257, Aug. 2019. [Online]. Available: <http://futureenergysp.com/index.php/tre/article/view/99/pdf>
- [25] A. G. Lazaropoulos, “Improvement of Power Systems Stability by Applying Topology Identification Methodology (TIM) and Fault and Instability Identification Methodology (FIIM)–Study of the Overhead Medium-Voltage Broadband over Power Lines (OV MV BPL) Networks Case,” *Trends in Renewable Energy*, vol. 3, no. 2, pp. 102-128, Apr. 2017. [Online]. Available: <http://futureenergysp.com/index.php/tre/article/view/34>
- [26] A. G. Lazaropoulos, “Detection of Energy Theft in Overhead Low-Voltage Power Grids – The Hook Style Energy Theft in the Smart Grid Era,” *Trends in Renewable Energy*, vol. 5, no. 1, pp. 12-46, Oct. 2018. [Online]. Available: <http://futureenergysp.com/index.php/tre/article/view/81/pdf>

Article copyright: © 2020 Athanasios G. Lazaropoulos. This is an open access article distributed under the terms of the [Creative Commons Attribution 4.0 International License](https://creativecommons.org/licenses/by/4.0/), which permits unrestricted use and distribution provided the original author and source are credited.



Technical Overview of the Net Metering in Lebanon

Issam Shabani*, Mohammad Chaaban*

Department of Industrial Engineering, Faculty of Technology, Lebanese University, Lebanon

Received October 6, 2020; Accepted October 21, 2020; Published October 28, 2020

In order to realize the best practices to allow the individuals participate in renewable energy production, a collection of legislation was ratified, and a set of decisions was introduced to encourage the prosumer concept. This notion, which is called Net Metering (NEM), is a billing mechanism that credits PV solar system owners for the energy injected to the grid. Lebanon adopts the NEM policy to reduce the demand and boost the grid through increasing the generation capacity. The decline of solar equipment cost encourages people to subscribe to the NEM service by utilizing the PV solar systems. The implementation of the NEM service provides the customers with leverage over their electricity bills. However, connecting the home micro grid into the vast grid is not easy. It imposes many technical challenges which are discussed in this article.

Keywords: Net Metering; Solar PV System; Renewable Energy Resources; Sustainable Energy; On-Grid System; Hawaii Back Feed Problem

1. Administrative Requirements

A major support for the expansion of solar energy in Lebanon is the Net Metering NEM policy which has been adopted and approved by the Electricite du Liban (EDL) through Decision No. 318-32 / 2011. Its advantages include legal and technical simplicity, in addition to the free installation of the meter by EDL.

The currently available Net Metering scheme implemented in Lebanon allows the subscribers to reduce the monthly bills through ‘net consumption’ payments which are rolled over to the next billing cycle – in case of surplus – until the end of the fiscal / calendar year. And then EDL will reset the counter to zero to start all over. In this case, any energy surplus is not financially remunerated, but is considered as a contribution to EDL’s electricity production [1]. This implies that oversizing of the solar Photo Voltaic (PV) system to more than the average annual energy consumption will increase its initial cost, while the return will remain constant, subsequently raising the system's payback period.

1.1 Subscription

Any electricity subscriber can apply for energy NEM by filling out the net metering interconnection application (at the EDL website), and uploading it with all required documentation. Apart from the personal information, the application form includes the name of manufacturer and supplier, technical details of the components planned to be installed, as well as the contractor’s name. Finally, the site drawing, single line diagram, and equipment data sheet are attached.

2. Technical Overview of NEM

The useful benefit of the Renewable Energy System (RES) system is its capability to connect with the general electrical grid, which allows the owner to transfer surplus energy directly to the utility by using the NEM (Figure 1). All that you need in addition to the PV system installation is to replace the old unidirectional electromechanical meter with a new electronic bi-directional meter, which mounted by EDL after you have subscribed to this service.

Each installation can differ depending on the RES used (such as PV, wind, biomass, and hybrid).

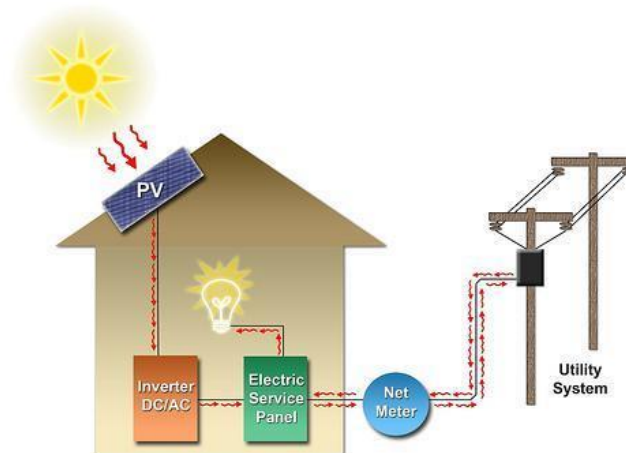


Figure 1. Residential Grid-Connected PV System with Net Metering
(www.slideshare.net/RaghavGupta20/zero-energy-building, Public Domain)

3. Applicable Standards

In order to ensure the installation's protection and safety from hazards, in addition to proper performance and efficiency, the PV installations should be in compliance with regulations (national or international regulations) and comply with different standards according to the country/region in which it is used. In the Lebanese context, inverters made in Europe are more common. However, a review of the applicable standards will help inform the decision-making process [2]. Lebanon has adopted the European standards that cover all issues related to PV systems and the NEM, such as the safety of power converters, environmental testing, measurement of photovoltaic current-voltage characteristics, the procedure for measuring efficiency, and characteristics of the utility interface (Figure 2).

Lebanon implemented the following European Standards (EN), VDE (part of the German standards collection) and IEC (The International Electro Technical Commission):

- ✓ IEC 61683: Photovoltaic systems – Power conditioners – Procedure for measuring efficiency.
- ✓ IEC 61727: Photovoltaic (PV) systems – Characteristics of the utility interface.
- ✓ IEC 62109-1-2: Safety of power converters for use in photovoltaic power systems.

- ✓ IEC 62116: Utility-interconnected photovoltaic inverters – Test procedure of islanding prevention measures.

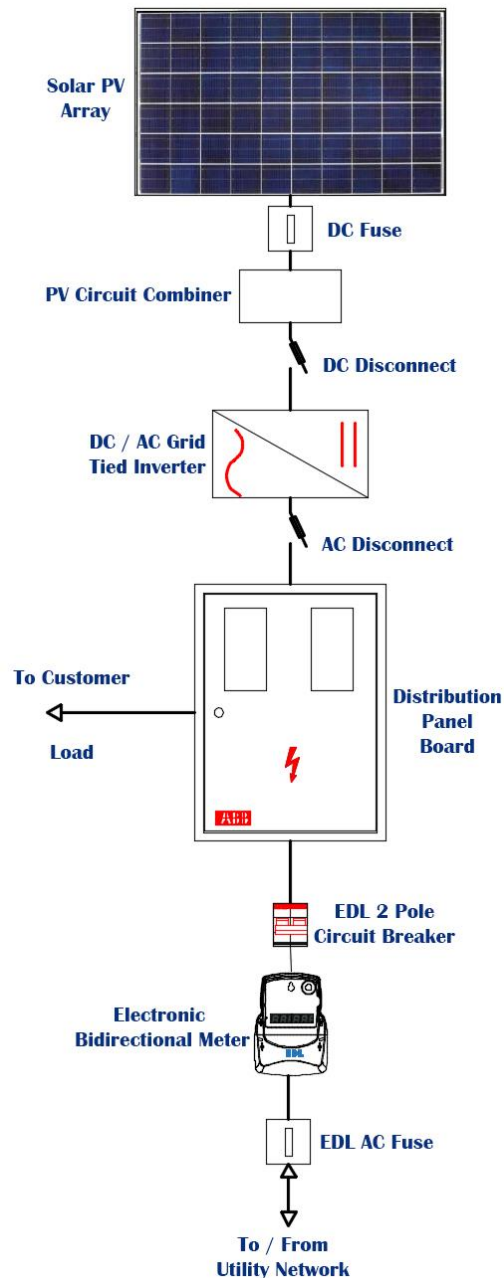


Figure 2. Single line diagram for NEM interconnection with no battery backup

- ✓ IEC 60068-2-5: Environmental testing – Part 2-5. Simulated solar radiation at ground level and guidance for solar radiation testing.
- ✓ IEC 60364-7-712: Electrical installations of buildings – Part 7-712. Requirements for special installations or locations – Solar photovoltaic (PV) power supply systems.
- ✓ IEC 60904-1: Photovoltaic devices – Part 1. Measurement of photovoltaic current-voltage characteristics.

- ✓ IEC 61683: Photovoltaic systems – Power conditioners – Procedure for Measuring efficiency
- ✓ IEC 61000-4-30: The method of measurement of grid quality parameters: frequency, voltage, harmonics, unbalance and flicker.
- ✓ IEC 61724: Photovoltaic system performance monitoring – Guidelines for measurement, data exchange and analysis.
- ✓ IEC 61727: Photovoltaic (PV) systems – Characteristics of the utility interface.
- ✓ IEC 61730-2: Photovoltaic (PV) module safety qualification – Part 2. Requirements for testing.
- ✓ IEC 61730-2: Photovoltaic (PV) module safety qualification – Part 2. Requirements for testing.
- ✓ IEC 62670-1: Photovoltaic concentrators (CPV) – Performance testing – Part 1. Standard conditions.
- ✓ IEC 62670-2: Photovoltaic concentrators (CPV) – Performance testing – Part 2. Energy measurement.
- ✓ VDE V 0126-1-1: Automatic disconnection device between a generator and the public low-voltage grid.
- ✓ EN 50438: Requirements for micro-generating plants to be connected in parallel with public low-voltage distribution networks.

4. Controllers

If you install an off-grid Renewable Energy System (*e.g.*, wind and PV) with a battery attached, you will need a charge controller. In our study, we mainly refer to PV charge controllers or solar charge regulators. The purpose of using them is to control the power from the solar array entering the battery bank. For this function, the controller is one of the most critical components in any power system.

The controllers protect the batteries from:

- ✓ **Over Charging**: A PV controller prevents overcharging of batteries by reducing the flow of energy to them (*i.e.*, opening the circuit between the battery and the PV array). Once a certain preset voltage is reached, this predetermined voltage can be adjusted by some types of controllers. If the voltage drops when the load increases, the controller will allow charging, which is known as voltage regulation.
- ✓ **Over Discharging**: Low Voltage Disconnect (LVD) circuit (included in the controller) will disconnect all loads when the battery discharges about 80% of its total capacity. This feature protects the batteries from complete discharge which damages them and reduces their lifespan. At night, in the absence of solar irradiation, the controller intervenes to prevent the current from flowing in the reverse direction, causing the batteries to drain.

Before purchasing a new controller, you may try to select it according to:

Adjustable set points – over current protection - reverse current protection – high / low voltage warning and protection, etc.

When a homeowner decides to install an on-grid PV solar system with a storage battery bank, there is no need to install a charge controller. Because the Grid-Tie Inverter is sufficient to direct the excess charge to the grid and protect the batteries from overcharging.

For the off-grid system, there are two types of charge controllers to consider: Pulse Width Modulation (PWM) controllers, and Maximum Power Point Tracking (MPPT) controllers.

4.1 Pulse Width Modulation (PWM) Technique

The Pulse Width Modulation (PWM) charge controller is used instead of the On-Off charging mode (old idea) which causes the battery plates to sulfate and reduces the nominal battery capacity by 55% to 60% after one year of usage. Sulfation happens inside lead-acid batteries when the electrolyte starts to break down due to incorrect charging levels and settings.

PWM charge controllers are solid state controllers that use a semiconductor switching element between the PV array and the battery. This element is switched on/off by PWM at a variable frequency determined by the variable duty cycle to maintain the battery at or very close to the voltage regulation set point. At this point the charging algorithm slowly reduces the charging current to avoid heating and gassing of the battery [3]. The charging cycle process continues to provide the battery with the full amount of energy in the shortest possible period. This results in improved overall performance, and a healthy battery with a longer life span.

PWM controllers are ideally suitable for small solar systems with a few low voltage PV solar panels and a small battery. They are simpler than MPPT controllers, and therefore typically less expensive.

4.2 Maximum Power Point Tracking (MPPT)

The extraction of the maximum available power from a photovoltaic module and substantially increasing the efficiency can be done by using the Maximum Power Point Tracking (MPPT) Controller [4]. Solar MPPT charge controllers are DC to DC converters that detect and convert the PV generated voltage to a more suitable one in real time basis. This operation can be achieved by tracking the maximum voltage-current (VI) value so that the system can charge the battery bank with the optimum power output (Figure 3).

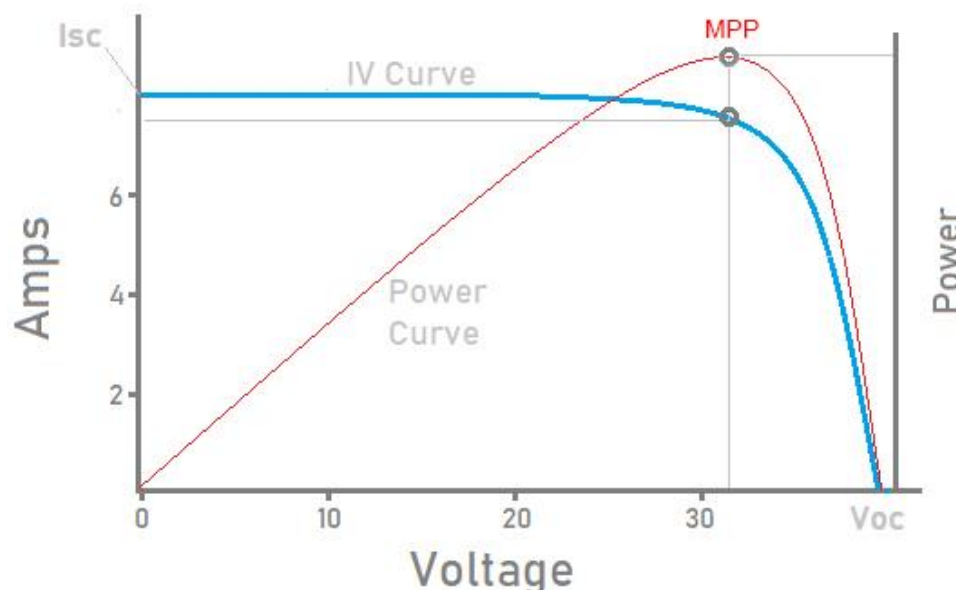


Figure 1. Current-Voltage-Power Characteristic Curve of a PV Module

The output power from the PV system is influenced by the weather conditions (*i.e.*, MPP is not fixed), and the maximum power varies proportionally with solar radiation and inversely with ambient temperature (non-linear relation). The MPPT charge controller is more effective and provides more power under these conditions:

- ✓ Cloudy or hazy ambient (very low irradiance).
- ✓ Cold days.
- ✓ The solar cell temperature is below 45°C or above 75°C.

As a result, using the MPPT controller gives you a 20% to 45% power gain in winter and 10-15% in summer and cost more money.

4.3 MPPT vs. PWM Controllers Economic Evaluation

The function of the solar charge controller is to regulate the power provided to the batteries from the PV panels. Overloading batteries can reduce the battery life and in some cases destroy them. PWM and MPPT solar charge controllers are commonly used to charge batteries with the solar power.

In the example below, a common 60 cell Polycrystalline Silicon PV panel with an operating voltage of 31.1 V and current 8.37 A is connected to a 12 V battery (Figure 4). To compare the performance of different types of controllers, we will use:

- PWM charge controller (1st case), with a price of 45\$ in the Lebanese market.
- MPPT charge controller (2nd case), with a price of 140\$ in the Lebanese market.

PHOTOVOLTAIC MODULE		
Solar Module Type : JKM260PP-60		
Maximum Power	(P _{max})	260W
Power Tolerance		0~+3%
Maximum Power Voltage	(V _{mp})	31.1V
Maximum Power Current	(I _{mp})	8.37A
Open Circuit Voltage	(V _{oc})	38.1V
Short Circuit Current	(I _{sc})	8.98A
Nominal Operating Cell Temp	(NOCT)	45±2°C
Maximum System Voltage		1000VDC
Maximum Series Fuse Rating		15A
Operating Temperature		-40°C~+85°C
Application Class		A
Fire Class		C
Weight		19.0(kg)
Dimension		1650×992×40(mm)
STC: 1000W/m ² , AM1.5, 25°C		

WARNING
 ONLY qualified personnel should install or perform maintenance work on these modules
 BE AWARE of dangerous high DC voltage when connecting modules
 DO NOT damage or scratch the rear surface of the module

Logos: TÜV Rheinland, CE, and a square symbol.

Figure 2. Polycrystalline Silicon PV panel

1st Case: PWM

Using the PWM charge controller (Figure 5), the panel voltage drops to 12 V to match the battery voltage, and as a result the power output is reduced to $8.37 \text{ A} \times 12 \text{ V} = 100 \text{ W}$.

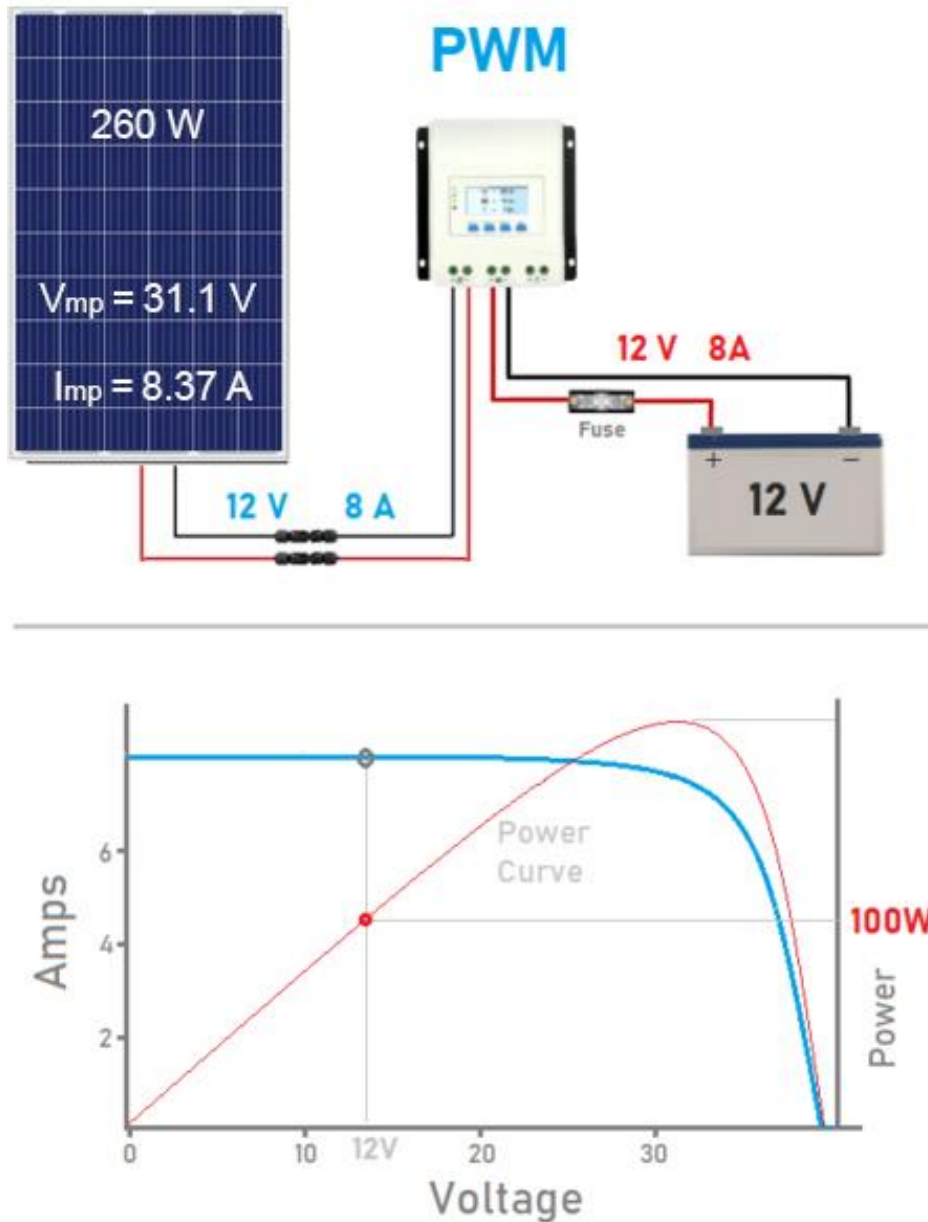


Figure 5. Power Drawn from PV Panel when Using PWM Controller.

2nd Case: MPPT

Using the MPPT charge controller, the PV panel can operate at its maximum power point (MPP), and produce much more power (Figure 6).

The power drawn from the panel is $8.37 \text{ A} \times 31.1 \text{ V} = 260 \text{ W}$.

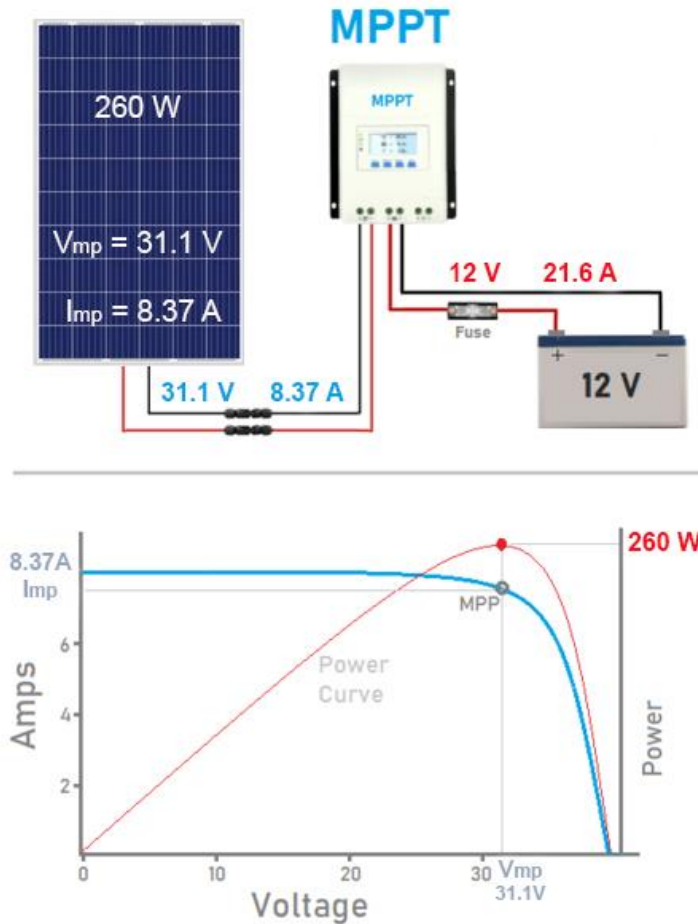


Figure 6. Power Drawn from PV Panel when Using MPPT Controller

To compare the obtained results, some assumptions are made (Table 1):

- The PV panel is in full sun.
- Controllers run with the maximum capacity.
- Ignore the presence of wires voltage drop.
- Continuous loading prevents the battery from a full charge.
- No maintenance needed for the controllers.
- The average daily sun is 6 hours (daily charging time).
- Sunny days are 300 days/year.

$$\text{Daily } \Delta P = \frac{(100W \cdot 6 \text{ hours}) / 1000}{(260W \cdot 6 \text{ hours}) / 1000} \times 100 = 38.4\%$$

The MPPT controller is better than the PWM controller by 38.4%.

Annual energy charged to the battery (PWM) = $100 \text{ W} \times 6 \text{ hours} \times 300 \text{ days} = 180 \text{ kWh}$.

Annual energy charged to the battery (MPPT) = $260 \text{ W} \times 6 \text{ hours} \times 300 \text{ days} = 468 \text{ kWh}$.

Average EDL electrical energy price = 9.5 cent/ kWh.

Energy savings per year = $468 \text{ kWh} - 180 \text{ kWh} = 288 \text{ kWh}$ annually.

Annual Savings = $288 \text{ kWh} \times 9.5 \text{ cent/ kWh} = 27.36 \text{ \$}$ annually.

$$\text{Simple Payback Period (SPB)} = \frac{\text{Initial Investment}}{\text{Annual Net Savings}} = \frac{120 \text{ \$}}{27.36 \text{ \$}} \cong 4.4 \text{ years.}$$

The latter analysis clearly indicates that using an MPPT controller improves energy harvesting by 38.4%. The MPPT controller may be a little bit expensive, but it does have a better efficiency, resulting in a valuable savings of about 27.36 \$/year. Finally, the 4.4 years SPB indicates that this investment is feasible, knowing that the average lifespan period of the system is 25 years.

Table 1. Comparing MPPT and PWM controllers.

MPPT Type Solar Controllers	PWM Type Solar Controllers
Algorithm included in the controller used to track maximum available power from the module.	Turn on and off to match the output voltage to the voltage needed by the battery.
New technology with increase in charging efficiency about 30%.	Old technology with moderate charging efficiency.
More expensive (2 – 3 times price of a comparable PWM controller).	Relatively low cost.
more sophisticated (more electronic components).	fewer electronic components.
Better in cool climate.	It performs well in warm temperatures.
Shorter lifespan due to greater thermal stress.	Longer lifespan due to low thermal stress.
Used when solar array voltage is higher than the battery voltage.	The Solar nominal voltage must match the battery bank nominal voltage.
Bigger in physical size, used for large systems.	Smaller size, used for smaller systems.

5. Inverters

There are two main operation modes of inverters, namely stand-alone (or off-grid) inverter, and grid connected (or grid-tie) inverter.

5.1 Stand-Alone Inverter

The stand-alone or off-grid power inverter is an electronic device that converts direct current (DC) from the battery to alternating current (AC) used by common appliances. Their size and rating range from a few hundred watts (small appliances) to megawatts, depending on the intent of use.

The main function of the inverter is to keep a constant voltage on the AC side and convert the input power, P_{in} into the output power, P_{out} with the highest possible efficiency [5], given by:

$$\eta_{inv} = \frac{P_{out}}{P_{in}} = \frac{V_{ac} I_{ac} \cos \varphi}{v_{dc} I_{dc}}$$

where

$\cos(\varphi)$ = power factor.

I_{dc} = current required by the inverter from the DC side, *i.e.*, controller (A).

V_{dc} = input voltage for the inverter from the DC side, *i.e.*, controller (V).

The quality of the inverter output waveform determines its performance. Normally, a sinusoidal waveform provides the best efficiency. There are three major different types of inverters, based on the shape of their output waveform:

- ✓ Square Wave Inverter.
- ✓ Modified Sine Wave Inverter.
- ✓ Sine Wave Inverter.

Square Wave Inverter

The square wave inverter is the simplest among all types. It is also the cheapest type of inverters, and least used. A simple oscillator can be used to produce square wave voltage. This waveform can run simple devices with a universal motor.

Most of the appliances are designed to use the sine waveform supply. If they are powered by a square wave, they can:

Get hot– buzz or make annoying humming noise – operate with very high losses - may be damaged. For these reasons, the square wave inverters are banned in a few European countries.

Modified Sine Wave

A modified sine wave or quasi sine wave inverter is designed to simulate a real sine wave, since the generation of the sine waves is expensive. It has a waveform more like a square, but with an extra step. It can operate most appliances but with reduced efficiency. Most motors will use about 20% more power and may create humming noises.

Sine Wave

“Pure” or “real” sine wave inverters are capable of simulating precisely the AC power that is generated by rotating AC machinery and are therefore supplied by the local utility company. This waveform is ideal for transforming the AC power with minimum harmonic distortion. The main benefit of this inverter is that most electrical and electronic appliances and equipment are designed to work well using sine-wave. Generally speaking, because of the additional circuitry, sine wave inverters are usually more costly (from 2 to 3 times) than other types.

Sizing Stand-Alone Inverter

The size of the stand-alone (off-grid) inverter depends on the total power of the connected appliances, which can be achieved by simply adding the rating of each connected device. If an electrical motor is attached, a high starting current is drawn for a limited time interval, so this should be taken into consideration when choosing the correct inverter protection. It shall be known that they are designed to withstand a surge for a few seconds.

5.2 Grid-Tie Inverter (GTI)

Unlike the stand-alone solar systems, on-grid PV systems are connected to the public network without the need for electrical storage devices (*i.e.*, virtually the grid is your battery). Any excess power that is not consumed by your electrical loads is exported into the utility company grid, which causes the meter to spin backward. Usually, you get returns for this energy.

The key role of the grid-interactive or synchronous inverters or simply the grid-tie inverter (GTI) is to synchronize the phase, voltage, and frequency of the power line with that of the grid (50 Hz grid frequency and 220 V root mean square voltage – nominal values of Lebanon electrical grid). When this matching happens, you can never notice anything. Similar to any dynamic system, the power system is continuously subjected to perturbations and experiences transitions from one operating point to another in the form of oscillations. Voltage stability, frequency stability, and inter-area oscillations have become greater concerns than in the past [6]. At any moment, the output voltage remains slightly higher than the grid voltage, so that excess electricity flows towards the grid.

A high-quality modern GTI has a fixed unity power factor, which means its output voltage and current are perfectly lined up and its phase angle is within 1 degree of the AC power grid. The GTI has an on-board computer that senses the current AC grid waveform, and outputs a voltage to correspond with the grid [7]. For these reasons, GTIs have various technical specifications and a complex constructional architecture that justifies their high price which is about three times the stand-alone inverter.

Installation Location

Like all electronic devices, GTIs run more efficiently in a cool environment. In order to optimize its lifetime and performance, the installation place should have the following specifications:

- Easily accessible cool spot.
- Away from direct sunlight
- Good ventilation.
- Away from moisture (dry place).
- Dust-free locked room.

Most of these mentioned requirements are not always available. As a result, the majority of GTIs are designed for outdoor use, with protection from rain, sleet, snow, water splashing, dust, and corrosion with optimum Ingress Protection (IP 65)¹. Ingress Protection rating, which is established by international standards, describes the level of sealing effectiveness of the enclosure against foreign bodies such as moisture and dust.

Sizing Grid-Tie Inverter

The size of the Grid-Tie inverter can be determined by knowing how much power will be drawn from PV panels or other RES such as wind turbines. It should take into consideration the surge (peak power produced by the solar system), which accounts for around 25% of the total power of the solar array.

There is no need to install charge controllers or battery banks in a grid-tied network but use GTIs instead. They are connected directly to the main grid and transform the DC power from a PV system to the AC power, thereby supplying power to the main grid and

reducing the electricity extracted from it. Some GTIs are hybrids which inject power to the grid and charge a battery bank for energy back up.

The output of a solar PV varies depending on the weather condition, irradiation, angle of incidence, and cell temperature. In order to maintain the efficient operation despite environmental variations, one approach is to use a maximum power point tracking (MPPT) algorithm to dynamically tune either control current or voltage to the maximum power operating point [8]. This feature is employed to optimize the system to work always at its maximum efficiency under any weather condition.

5.3 Total Harmonic Distortion (THD)

The phrase “Power Quality” has been widely used during the last decade and includes all aspects of events in the system that deviates from normal operation. However, it is more correct to distinguish between voltage and current quality, rather than power quality [9]. To improve the reliability of the grid, the wave distortions should be prohibited, which increase the peak current, reduce the power factor, and thus result in lower efficiency due to higher temperature.

In normal conditions, the output voltage form is a sinusoidal wave where THD is close to or equal to zero. THD is the percentage value between the total components of harmonics (voltage or current) with its fundamental components. The greater the percentage of THD, the greater the risk of equipment damage [10].

$$\begin{aligned}
 THD &= \sqrt{\sum_{h=2}^h \left(\frac{Q_h}{Q_1}\right)^2} \\
 &= \frac{\sqrt{(V_2 + V_3 + V_4 + \dots \dots V_h)^2}}{V_1} * 100\%
 \end{aligned}$$

where

Q represents either current or voltage.

Q_1 = r.m.s. value of the fundamental component.

h = harmonic order. Harmonic: is a multiple of the basic frequency 50 Hz; the 2nd harmonic is at 100 Hz; the 3rd harmonic at 150 Hz, etc. These harmonic waveforms are added to the basic which creates a distorted sine wave.

Q_h = r.m.s. value of the harmonic component of order h.

The nominal output voltage waveform of the PV power Plant shall be of 230/400 V, 50 Hz, with a sinusoidal waveform complying with a THD < 5%. For plants with an output current $I \leq 16$ A per phase, the harmonic components of the current produced and measured at the output terminals shall comply with the standard IEC 61000-3-2 “Electromagnetic compatibility (EMC) - Part 3-2: Limits - Limits for harmonic current emissions (equipment input current ≤ 16 A per phase)”. The limitation of voltage changes, voltage fluctuations, and flicker shall comply with the standard IEC 61000-3-3. For all the plants connected to the low voltage (LV) grid, the voltage quality measured at the Point of Connection shall be in accordance with the IEC 61000-2-2 “Compatibility levels for low-frequency conducted disturbances and signaling in public low-voltage power supply systems” and IEC/TR 61000-3-14 [2].

5.4 Islanding

Distributed Generation is a system that produces electricity near the consuming area. The condition of “Islanding” in Distributed Generators (DGs) is an electrical phenomenon that occurs when the energy supplied by the power grid is interrupted due to various factors and the DGs continue energizing some or the entire load. Thus, the power grid stops controlling this isolated part of the distribution system, which contains both loads and generation [11]. Islanding is often considered as an undesirable event because of the potential damage to existing equipment, utility liability concerns, reduction of power reliability, and power quality [12].

For these purposes, DGs systems must sense islanding and automatically (fast response time) detach it from the circuit; this is referred to as anti-islanding. GTIs were equipped with anti-islanding features to easily and quickly disconnect DG from the grid in order to reduce risks when the power grid goes down (blackout). It will shut down quickly to stop the electricity from passing through it to avoid harming any maintenance worker who is repairing the power grid and has the ability to restore its normal operation when the main grid is switched on again.

To prevent islanding, several detection methods have been used to monitor over/under voltage and over/under frequency. The European general practice is to keep PV inverters connected during minor faults in order to support the grid riding through voltage dips and operating at variable reactive power levels to maintain normal grid voltage [13]. According to the country or region, different standards have been adopted. The European standard is the guide in Lebanon. The licensed inverter should be compliant with the IEC 62116 standard (Utility-interconnected photovoltaic inverters – Test procedure of islanding prevention measures) and can be configured with the following parameters [14]: Loss of main detection limit of 300 ms.

6. Hybrid Solar Systems

Most NEM subscribers do not use batteries, as the output of excess power generation goes to the grid. If the grid goes into power outage or becomes unstable (case repeated in Lebanon every day), your home will lose power, because the GTI will shut down entirely for safety reasons. To overcome the utility power failure problem, you can use a backup battery bank, and get power temporarily from batteries in a battery ready system.

Hybrid solar systems take the benefits of both grid-tied (NEM) and off-grid (battery bank charging) solar systems. To do so, you will need a special hybrid solar inverter or just connect a charge controller to the system. This type of inverter is capable of prioritizing various loads and different sources simultaneously (*i.e.*, feeding the load and charging the battery at the same time).

Hybrid solar system’s advantages:

- Less expensive than the off-grid solar system since the capacity of the battery bank can be less than the peak requirements.
- Keeping the power uninterrupted after the main grid failure (*i.e.*, continuous power supply).
- Benefits from the RES to the fullest because there is no waste of excess energy at the time of the blackout.

Hybrid solar system’s disadvantages:

- Higher initial cost of batteries and hybrid solar inverter.
- Higher maintenance expenses due to the presence of batteries.
- Longer payback period after the relative rise in CAPEX and OPEX.
- More complicated installation and wiring (need more room space).

7. Energy Metering

NEM allows energy to flow in two directions, *i.e.*, from the customer side to the grid when the supply is excessive and from the grid to the customer side when the demand is greater than the RE production. Bidirectional utility meters adopted for the NEM service are capable of recording how much net power consumed from the EDL grid, but cannot tell users how much power consumed from the PV solar system. To know the quantity of power generated from the solar system, another separated energy meter is required to be installed at the PV panels output. In this case, a dual energy metering system is implemented.

7.1. Standards and Norms

The EDL accepted meters shall be designed, manufactured and tested in conformity with the latest IEC standards and/or the corresponding national standards. In case of any deviation, the vendor/manufacturer may propose equipment/material conforming to equivalent national standards. However, the provisions of following specifications shall supersede the provisions of these standards in case of any conflict.

IEC-62052-11: Electricity metering equipment (a.c.)- General requirements, tests and test conditions.

IEC-62053-21: Electricity metering equipment (a.c.)- static meters for active energy(classes 1 and 2).

IEC-62054-21: Electricity metering – Tariff and load control – Particular Requirements for time switches.

IEC-62056-21: Electricity metering - Data exchange for meter reading, tariff and load control –Direct local data exchange.

IEC-60695-2-10: Fire hazard testing. Part-2 test methods glow wire test and guidance.

IEC-60947-7-1: Test requirements of Terminal Blocks.

IEC-62056-62: Electricity metering - Data exchange for meter reading, tariff and load control –Interface classes.

IEC-62056-42: Electricity metering - Data exchange for meter reading, tariff and load control –Physical layer.

IEC-62056-46: Electricity metering - Data exchange for meter reading, tariff and load control –Data link layer.

IEC-62056-53: Electricity metering - Data exchange for meter reading, tariff and load control –COSEM Application layer.

IEC-62056-61: Electricity metering - Data exchange for meter reading, tariff and load control –Object identification system (OBIS).

IEC-61334-4-41: Distribution Automation Using Distribution Line Carrier Systems–Part4.

7.2. Technical Specifications of Approved Energy Meter

EDL approved the installation of the electronic energy meters (Circutor – CIRWATT B series, made in Spain) into the NEM service customers system. These meters are intended for indoor installation and have the following specifications:

1. Single phase multi-function, multi tariff static meter with not less than four tariffs for kWh (daily, weekly, seasons, etc.), used for low voltage direct connection 1×230 volts 15/60 A, class (1) according to IEC 62053-21.
2. The meter has a reasonably dust-proof case, which can be sealed in such a way that the internal parts of the meter are accessible only after breaking the seals. The meter cover shall not be removable without removing seals and the use of a tool, and the base and cover materials should be quality insulating material (polycarbonate).
3. Minimum ambient temperature - 10°C, maximum ambient temperature 45°C, and 95% humidity.
4. Rated frequency 50 Hz, Rated voltage 230 volts, voltage variations 0.85 / 1.15 of rated voltage, and rated current up to 60 A.
5. The meter conformed to the degree of protection IP 51, as given in IEC 60529; the meters are well protected against moisture and direct entry by an excellent system of seals, gaskets, interlocking grooves, and channels moldings.
6. The meter data stored in non-volatile memory (EEPROM: Electrically Erasable Programmable Read-Only Memory) and can be read manually from the meter with a portable PC or a hand-held terminal. The meter has a memory sufficient to store at least 90 days of Load profile.
7. The meter incorporates a digital display unit, which displays: import active energy kWh, export active energy kWh, current in Amp, Voltage, error code, date and time.
8. The configuration software runs on windows operating environment. This software has two level of permissions:
 - Administrator level: the administrator can do all tasks and define Users and give them the permissions and tasks.
 - Operator level: the operator can do only tasks determined by administrator.

8. Summary and Technical challenges

EDL is unable to meet the demand because of insufficient generation capacities, especially during peaks. Since it has high solar energy potential due to irradiation levels, Lebanon adopts the NEM policy to reduce the demand and boost the grid through increasing the generation capacity. The decline of solar equipment cost, encourage people to subscribe to the NEM service by utilizing the PV solar systems. The implementation of the NEM service gives the customer some leverage over his electricity bill, but too many administrative and financial steps are required to apply. Connecting your home micro grid into the vast grid is not easy; but rather imposes many technical challenges.

8.1. Frequent Power Outages

When the grid goes into power blackout, your home will lose power, which is the main issue that concerns NEM customers. Due to the frequent blackouts in the national electricity network, backup batteries are needed and are considered essential to the functioning of net metering in Lebanon [15]. Because of this, hybrid solar systems take the

advantages of both grid-tied (NEM) and off-grid systems and are recommended to be used in Lebanon to overcome the problem of Frequent Power Outages.

A dual-type inverter with special settings harmonized with the Lebanese grid parameters is needed to implement a hybrid solar system. The transfer relay that disconnects and reconnects the inverter to the grid can be either internal or external (Table 2). The dual inverter accepts a wider fluctuation of grid voltage and frequency than a purely grid-dependent inverter [13].

Table 2. Recommended settings for grid tied Inverter - CEDRO Project [13].

RECOMMENDED SETTINGS FOR INTERCONNECTED NET METERED RENEWABLE ENERGY MICRO POWER PLANTS WITH INVERTERS						
TYPE OF PLANT	REFERENCES DIAGRAM (SINGLE PHASE)	RATED CURRENT	DISCONNECTION MEANS	VOLTAGE TOLERANCE	FREQUENCY TOLERANCE	TRIP DISCONNECTION TIME
B1: Grid dependent		Nominal power ($<$ subscribed demand)	-Inverter embedded stop function -Inverter external switch -External Transfer switch	$> 0,80 U_m$ $< 1,15 U_m$	$> 45 \text{ Hz}$ $< 55 \text{ Hz}$	$< 2s$

8.2. Frequency Fluctuations

Frequency drift, upwards or downwards, in a power system is the main indicator of the momentary imbalance between generation and demand. If at any instant, power demand exceeds supply, then the system frequency falls. Conversely, if the power supply exceeds demand, the frequency rises. The system frequency fluctuates continuously in response to the changing demand and due to the practical impossibility of generation being controlled to instantaneously track all changes in demand [16]. Future power system security will be challenged by the increasing penetration of non-synchronous RES. With high penetration levels of RES, the power system's dynamic complexity increases, and the system frequency control becomes a challenging task [17].

In the case of Lebanon, the frequency of the grid is always fluctuating due to high demand and lack of electricity supply. The National Control Center (NCC) dispatchers in EDL often seek to manually handle and monitor grid frequency variations by switching on and off some medium voltage feeders. These interventions from the dispatchers are relatively slow and cause some disturbances to the electrical network. Any severe or sudden increase or decrease in frequency will cause a partial or total collapse of the grid (total blackout).

8.3. Voltage Instability

Voltage stability of networks is still a major issue with major blackouts having recently occurred. Voltage stability refers to the capability of the power system to sustain constant voltage at all buses after being subjected to a disturbance from a given initial operating point [18].

Voltage disturbances are swings in supply voltage, which may be small due to marginal load switching and may be significant due outage of generation machine or presence of traveling surge on the power lines. Such changes would negatively affect the performance of the appliances (like light dimming or inability of starting an induction motor). The effect depends mainly on the value and the duration time of the change.

8.4. Electrical Back Feed (Hawaii Case)

The incentive policy of Hawaii Electrical CO. has set up a generous NEM program, which leads to the overbuilding of PV systems. Because the peak solar power production

occurs around mid-day between 10:00 and 14:00, causing the grid to be flooded with solar electricity. The grid is not designed to deal with such a situation. In 2013, Hawaiian Electrical network is experienced enough PV solar coming onto an increasing quantity of circuits to back-feed power into their distribution grid on sunny days, and to drive system-wide demand curves below zero on peak days. Excess energy from a high influx of PV can back-feed into the circuits, causing overvoltage, reverse overloading, and other problems [19]. This over generation increased the voltage on the power lines and caused disturbances on household appliances and the utility's equipment.

This drop in demand highlighted the solar surplus that was sent to the grid, showing the difference in electricity demand and the supply from solar energy throughout the day. Solar generation in several US states (California and Arizona etc.) has started to cause significant variations in supply and demand curves. The result is drawing a “duck curve” (sometimes the duck's belly hits bottom).

In 2015, the Hawaiian Electric Co. decided to stop offering the state's most popular solar incentive program of NEM, which credits solar owners the full retail rate for any excess energy their systems send to the grid and replaced the NEM program with less attractive options [20].

CONFLICTS OF INTEREST

The authors declare that there is no conflict of interests regarding the publication of this paper.

REFERENCES

- [1] United Nations Development Programme (UNDP) / CEDRO. (2018). *Sustainable Energy for Lebanese Villages and Communities: The Village 24 Initiative*. <https://data2.unhcr.org/en/documents/details/66473> (accessed on 10/26/2020)
- [2] United Nations Development Programme (UNDP) / CEDRO. (2017). *Guidelines On Net - Metering: The Case Of Lebanon*. <https://data2.unhcr.org/en/documents/details/65011> (accessed on 10/26/2020)
- [3] Qazi, S. (2017). Chapter 2 - Fundamentals of Standalone Photovoltaic Systems. In: *Standalone Photovoltaic (PV) Systems for Disaster Relief and Remote Areas*, S. Qazi, ed., Elsevier, pp: 31-82. DOI: 10.1016/B978-0-12-803022-6.00002-2.
- [4] Pakkiraiah, B., and Sukumar, G. D. (2016). Research Survey on Various MPPT Performance Issues to Improve the Solar PV System Efficiency. *Journal of Solar Energy*, 2016, 8012432. DOI: 10.1155/2016/8012432.
- [5] Kalogirou, S. A. (2013). *Solar energy engineering: processes and systems*, Academic Press..
- [6] Eremia, M., and Shahidehpour, M. (2013). *Handbook of electrical power system dynamics: modeling, stability, and control*, John Wiley & Sons.
- [7] Shertukde, H. M. (2017). *Distributed Photovoltaic Grid Transformers*, CRC Press.
- [8] Brunton, S. L., Rowley, C. W., Kulkarni, S. R., and Clarkson, C. (2010). Maximum Power Point Tracking for Photovoltaic Optimization Using Ripple-

- Based Extremum Seeking Control. *IEEE Transactions on Power Electronics*, 25(10), 2531-2540. DOI: 10.1109/TPEL.2010.2049747.
- [9] Lundquist, J. (2001). *On harmonic distortion in power systems*. Chalmers University of Technology.
<http://citeseerx.ist.psu.edu/viewdoc/download?doi=10.1.1.531.4194&rep=rep1&type=pdf> (accessed on 10/26/2020)
- [10] Raharja, L. P. S., Arief, Z., and Windarko, N. A. J. E. I. J. o. E. T. (2017). Reduction of total harmonic distortion (THD) on multilevel inverter with modified PWM using genetic algorithm. 5(1), 91-118.
- [11] Trujillo, C., Velasco, D., Garcerá, G., Figueres, E., and Carranza, O. J. m. (2010). Analysis of Active Islanding methods for single phase inverters, in *International Conference on Renewable Energies and Power Quality*, Granada, Spain, 2010, pp. 1281-1286. DOI: 10.24084/repqj08.645
- [12] Wrinch, M. C. (2008). *Negative sequence impedance measurement for distributed generator islanding detection*. University of British Columbia
- [13] United Nations Development Programme (UNDP) / CEDRO. (2013). Photovoltaic Plants in Lebanon.
<http://www.databank.com.lb/docs/Photovoltaic%20plants%20in%20Lebanon-Cedro%202013.pdf> (accessed on 10/26/2020)
- [14] Lara, J. D. (2017). *Net Metering Guidelines for Lebanon*. <http://www.cedro-undp.org/content/uploads/event/170131112833676~Netmetering.pdf> (accessed on 10/26/2020)
- [15] The Lebanese Center for Energy Conservation (LCEC). (2016). *The National Renewable Energy Action Plan (NREAP) for the Republic of Lebanon 2016-2020*. http://lcec.org.lb/Content/uploads/LCECOther/161214021429307~NREAP_DEC14.pdf (accessed on 10/26/2020)
- [16] Short, J. A., Infield, D. G., and Freris, L. L. (2007). Stabilization of Grid Frequency Through Dynamic Demand Control. *IEEE Transactions on Power Systems*, 22(3), 1284-1293. DOI: 10.1109/TPWRS.2007.901489
- [17] Ahmadyar, A. S., Riaz, S., Verbic, G., Chapman, A., and Hill, D. J. J. a. p. a. (2017). *A Framework for Frequency Stability Assessment of Future Power Systems: An Australian Case Study*. arXiv:1708.00739 [cs.SY].
<https://arxiv.org/pdf/1708.00739.pdf> (accessed on 10/26/2020)
- [18] Heetun, K. Z., Abdel Aleem, S. H. E., and Zobaa, A. F. (2016). Voltage stability analysis of grid-connected wind farms with FACTS: Static and dynamic analysis. *Energy and Policy Research*, 3(1), 1-12. DOI: 10.1080/23317000.2015.1128369.
- [19] GRID20/20 Inc. (2018). *Managing DER Impacts, The GRID20/20 OptaNODE® Solution enables continuous increase*.
https://grid2020.com/private_files/GRID2020_DER_Case_Study.pdf (accessed on 10/26/2020)
- [20] Cournoyer, C. (2016). *End of Hawaii's Solar Credit Program Spells Trouble for Industry*. <https://www.governing.com/topics/transportation-infrastructure/tns-hawaii-solar.html> (accessed on 10/26/2020)

Article copyright: © 2020 Issam Shabani and Mohammad Chaaban. This is an open access article distributed under the terms of the [Creative Commons Attribution 4.0 International License](https://creativecommons.org/licenses/by/4.0/), which permits unrestricted use and distribution provided the original author and source are credited.





CALL FOR PAPERS

Trends in Renewable Energy

ISSN Print: 2376-2136 ISSN online: 2376-2144

<http://futureenergysp.com/index.php/tre/>

Trends in Renewable Energy (TRE) is an open accessed, peer-reviewed semi-annual journal publishing reviews and research papers in the field of renewable energy technology and science. The aim of this journal is to provide a communication platform that is run exclusively by scientists. This journal publishes original papers including but not limited to the following fields:

- ✧ Renewable energy technologies
- ✧ Catalysis for energy generation, Green chemistry, Green energy
- ✧ Bioenergy: Biofuel, Biomass, Biorefinery, Bioprocessing, Feedstock utilization, Biological waste treatment,
- ✧ Energy issues: Energy conservation, Energy delivery, Energy resources, Energy storage, Energy transformation, Smart Grid
- ✧ Environmental issues: Environmental impacts, Pollution
- ✧ Bioproducts
- ✧ Policy, etc.

We publish the following article types: peer-reviewed reviews, mini-reviews, technical notes, short-form research papers, and original research papers.

The article processing charge (APC), also known as a publication fee, is fully waived for the Trends in Renewable Energy.

Call for Editorial Board Members

We are seeking scholars active in a field of renewable energy interested in serving as volunteer Editorial Board Members.

Qualifications

Ph.D. degree in related areas, or Master's degree with a minimum of 5 years of experience. All members must have a strong record of publications or other proofs to show activities in the energy related field.

If you are interested in serving on the editorial board, please email CV to editor@futureenergysp.com.